

---

Masters Theses

Student Theses and Dissertations

---

Spring 2016

## Phase field modeling of electrodeposition process in lithium metal batteries

Nihal Acharya

Follow this and additional works at: [https://scholarsmine.mst.edu/masters\\_theses](https://scholarsmine.mst.edu/masters_theses)



Part of the [Materials Science and Engineering Commons](#)

Department:

---

### Recommended Citation

Acharya, Nihal, "Phase field modeling of electrodeposition process in lithium metal batteries" (2016). *Masters Theses*. 7491.

[https://scholarsmine.mst.edu/masters\\_theses/7491](https://scholarsmine.mst.edu/masters_theses/7491)

This thesis is brought to you by Scholars' Mine, a service of the Missouri S&T Library and Learning Resources. This work is protected by U. S. Copyright Law. Unauthorized use including reproduction for redistribution requires the permission of the copyright holder. For more information, please contact [scholarsmine@mst.edu](mailto:scholarsmine@mst.edu).

PHASE FIELD MODELING OF ELECTRODEPOSITION PROCESS IN LITHIUM  
METAL BATTERIES

by

NIHAL ACHARYA

A THESIS

Presented to the Faculty of the Graduate School of the  
MISSOURI UNIVERSITY OF SCIENCE AND TECHNOLOGY

In Partial Fulfillment of the Requirements for the Degree

MASTER OF SCIENCE IN MATERIALS SCIENCE & ENGINEERING

2016

Approved by:

Dr. Mohsen Asle Zaeem, Advisor  
Dr. Michael Moats  
Dr. Caizhi Zhou

© 2016

Nihal Acharya

All Rights Reserved

## ABSTRACT

One of the main weaknesses in long term performance of conventional lithium batteries is the growth of lithium microstructures on the electrode surface due to an electrochemical process, which can eventually lead to failure of these batteries. Suppressing this microstructure growth is a key in developing new generations of lithium metal batteries (LMBs). In this study, a two-dimensional (2D) phase field model is constructed to understand and determine the parameters controlling formation and evolution of microstructures in LMBs. A Ginzburg-Landau free energy functional, which is a function of concentration of  $\text{Li}^+$  and applied voltage, and a system consisting of a pure lithium metal electrode and an electrolyte made of lithium hexafluorophosphate in a binary organic solvent of 1:1 ratio of ethylene carbonate and dimethyl carbonate. The evolution equations consist of a Cahn-Hilliard fourth-order partial differential equation (PDE) for evolution of  $\text{Li}^+$  concentration in the domain, and a Laplace's equation for charge conservation. Using COMSOL, the growth thickness and growth rate from the anode surface are simulated by applying different boundary conditions of concentration and different potentials. The proposed model is compared to existing electrodeposition models and results show that the Laplace's equation can be used in different forms proposed in literature. Assuming this battery to be a strongly anisotropic system, the Cahn-Hilliard equation is modified to include anisotropy and the simulations reveal a strong directional growth from the anode surface. The results of the developed model suggested that this phase field model is capable of quantitatively predicting the formation and growth of microstructures in LMBs and may be used to improve their life time in the future. This model can also be applied to study electrodeposition process in other material systems.

## ACKNOWLEDGEMENTS

Firstly, I would like to extend my most sincere gratitude to my advisor, Dr. Mohsen Asle Zaeem. He has been very supportive and patient with me. He has always found time to listen to me, guide me through every roadblock and has been an extremely good teacher. His guidance and technical expertise have been pivotal in helping me complete this research effort, which has been a truly enlightening experience.

I would like to thank the members of my committee, Dr. Michael Moats and Dr. Caizhi Zhou for their time and valuable insights to help augment the quality of this work.

I would like to thank NASA-EPSCoR for funding this research effort.

I'm grateful to everyone in the Materials Science & Engineering department here at Missouri S&T, for the informative seminars every Thursday and social events like ATF parties, Christmas Lunches and "pie-ing", where I got to know many people personally.

I was blessed to be a part of a wonderful research group – Mohsen, Mahdi, Jake, Ebrahim, Arezoo, Lieren and Ning – and through discussions with them, I have learnt a great deal about and beyond the scope of my research.

I never would have made it this far without the blessings of my parents, Manorama and Gopal, and my grandparents Krishnacharya, Girimajirao, Damayanthi and Shalini, and I am forever indebted to them for supporting all my decisions. The friendships forged here at Missouri S&T will stand for years to come.

Lastly, a big thank you to the current squad at Arsenal Football Club, whose performances have been responsible for 75% of my happiness in the past year.

## TABLE OF CONTENTS

	Page
ABSTRACT.....	iii
ACKNOWLEDGEMENTS.....	iv
LIST OF ILLUSTRATIONS.....	ix
LIST OF TABLES.....	xii
 SECTION	
1. LITHIUM BATTERIES.....	1
1.1. BACKGROUND .....	1
1.2. CURRENT STATE OF THE ART IN LITHIUM BATTERY RESEARCH....	2
1.3. CURRENT STATUS AND FUTURE PROSPECTS .....	7
1.3.1. Lithium Sulfur Batteries.....	7
1.3.2. Lithium Air Batteries.....	8
1.4. SAFETY ISSUES .....	9
1.5. APPLICATIONS OF LITHIUM BATTERIES .....	11
1.6. SUMMARY .....	12
2. COMPONENTS OF THE LITHIUM BATTERY.....	13
2.1. ELECTROLYTES .....	13
2.1.1. Organic Solvents .....	14
2.1.2. Lithium Salts .....	17
2.1.2.1. Lithium perchlorate (LiClO <sub>4</sub> ).....	18
2.1.2.2. Lithium tetrafluoroborate (LiBF <sub>4</sub> ).....	18
2.1.2.3. Lithium hexafluoroarsenate (LiAsF <sub>6</sub> ).....	19
2.1.2.4. Lithium hexafluorophosphate (LiPF <sub>6</sub> ).....	19

2.1.2.5. Lithium bis (trifluoromethanesulfonyl)mide - Li[N(CF <sub>3</sub> SO <sub>2</sub> ) <sub>2</sub> ] or LiTFSI.....	20
2.2. SOLID ELECTROLYTE INTERFACE (SEI).....	20
2.3. ELECTRODES.....	21
2.3.1. Anode in Lithium Batteries. ....	23
2.3.1.1. Lithium metal anode.....	23
2.3.1.2. Intercalated lithium compound anode.....	23
2.3.2. Cathode in Lithium Batteries. ....	24
2.3.2.1. Lithium cobalt oxide (LiCoO <sub>2</sub> ).....	26
2.3.2.2. Lithium manganese oxide (LiMn <sub>2</sub> O <sub>4</sub> ).....	26
2.3.2.3. Lithium nickel oxide (LiNiO <sub>2</sub> ).....	26
2.3.2.4. Lithium iron phosphate (LiFePO <sub>4</sub> ).....	26
2.3.2.5. Composite cathodes.....	27
2.4. SUMMARY.....	27
3. COMPUTATIONAL MODELING TECHNIQUES FOR MICROSTRUCTURE EVOLUTION.....	28
3.1. UNDERSTANDING THE EVOLUTION OF MICROSTRUCTURES .....	28
3.2. SHARP INTERFACE MODEL .....	29
3.3. PHASE FIELD MODEL .....	30
3.4. SHARP INTERFACE MODEL VS. DIFFUSE INTERFACE (PHASE FIELD) MODEL .....	31
3.5. LIMITATIONS OF PHASE FIELD MODELS.....	33
3.6. SUMMARY.....	33
4. CURRENT PHASE FIELD MODELS OF ELECTRODEPOSITION PROCESS.....	34
4.1. PHASE FIELDS AND THEIR EVOLUTIONS .....	35
4.1.1. Conserved Order Parameter .....	37
4.1.2. Non-Conserved Order Parameter .....	38

4.1.3. The Ginzburg-Landau Free Energy Functional.....	39
5. PROPOSED PHASE FIELD MODEL FOR ELECTRODEPOSITION IN LITHIUM METAL BATTERIES .....	40
5.1. PROPOSED PHASE FIELD MODEL.....	40
5.2. GOVERNING EQUATIONS.....	43
5.2.1. Anisotropy in Cahn-Hilliard Equation .....	44
5.3. SIMULATION PARAMETERS AND BOUNDARY CONDITIONS .....	45
6. RESULTS AND DISCUSSIONS .....	48
6.1. CONVERGENCE STUDY .....	48
6.2. EFFECT OF DIFFERENT ELECTRICAL CONDUCTIVITY RATIOS .....	52
6.3. EFFECT OF DIFFERENT BOUNDARY CONDITIONS FOR CONCENTRATION FIELD.....	54
6.3.1. Zero Flux Boundary Condition for Concentration and Applied Voltages of 0.1V, 0.2V and 0.3V.....	55
6.3.2. Dirichlet Boundary Condition for Concentration and Applied Voltages of 0.1V, 0.2V and 0.3V.....	64
6.3.3. Constant Flux (Neumann) Boundary Condition for Concentration and Applied Voltages of 0.1V, 0.2V and 0.3V.....	68
6.4. COMPARISON WITH OTHER WORKS .....	72
6.5. EFFECT OF ANISOTROPY .....	77
6.6. DISCUSSIONS.....	82
6.7. FUTURE WORK.....	86
APPENDICES	
A. NON-DIMENSIONALIZATION PROCEDURE .....	88
B. INPUTS IN COMSOL MULTIPHYSICS .....	91
C. INPUTS IN COMSOL MULTIPHYSICS FOR ANISOTROPY .....	99
BIBLIOGRAPHY.....	102



VITA.....108

## LIST OF ILLUSTRATIONS

	Page
Figure 1.1. Comparison of different battery technologies in terms of energy densities.....	2
Figure 1.2. Dendrite growth on the anode surface of Li metal battery (top) and Li-ion battery (bottom) .....	6
Figure 1.3. Short circuiting in lithium cells .....	10
Figure 2.1. Ring structures of cyclic organic compounds used in lithium batteries.....	15
Figure 2.2. Chain structures of non-cyclic (linear) organic solvents used in lithium batteries .....	16
Figure 3.1. Graphical representations .....	32
Figure 4.1. Variation of order parameter interpolating function $p(\xi)$ .....	36
Figure 5.1. Free energy density without applied potential (blue curve) and with applied potential (red curve) of 0.1V vs. concentration.....	41
Figure 6.1. Element shapes used in 2D analysis.....	48
Figure 6.2. Element shapes used in 3D analysis.....	49
Figure 6.3. Thickness vs. (1/Mesh).....	52
Figure 6.4. Thickness vs different electrical conductivity ratios.....	54
Figure 6.5. Growth thickness vs. time for different applied voltages and zero flux of concentration.....	56
Figure 6.6. Thickness vs. applied voltage for zero flux of concentration.....	57
Figure 6.7. Growth rate vs. applied voltage for zero flux of concentration.....	58
Figure 6.8. Concentration profiles at $t=0$ (top), $t=0.808s$ (middle) and $t=1.616s$ (bottom) for zero flux boundary condition for $\phi=0.1V$ .....	60
Figure 6.9. Potential profiles at $t=0$ (top), $t=0.808s$ (middle) and $t=1.616s$ (bottom) for zero flux boundary condition for $\phi=0.1V$ .....	60
Figure 6.10. Potential profiles at $t=0$ and $t=1.616s$ for zero flux boundary condition for $\phi=0.1V$ .....	61

Figure 6.11. Concentration profiles at t=0 (top), t=0.808s (middle) and t=1.616s (bottom) for zero flux boundary condition for $\phi=0.2V$ .....	61
Figure 6.12. Potential profiles at t=0 (top), t=0.808s (middle) and t=1.616s (bottom) for zero flux boundary condition for $\phi=0.2V$ .....	62
Figure 6.13. Potential profiles at t=0 and t=1.616s for zero flux boundary condition for $\phi=0.2V$ .....	62
Figure 6.14. Concentration profiles at t=0 (top), t=0.808s (middle) and t=1.616s (bottom) for zero flux boundary condition for $\phi=0.3V$ .....	63
Figure 6.15. Potential profiles at t=0 (top), t=0.808s (middle) and t=1.616s (bottom) for zero flux boundary condition for $\phi=0.3V$ .....	63
Figure 6.16. Potential profiles at t=0 and t=1.616s for zero flux boundary condition for $\phi=0.3V$ .....	64
Figure 6.17. Growth thickness vs time for different applied potentials for Dirichlet boundary condition of concentration .....	65
Figure 6.18. Growth thickness vs applied voltage for Dirichlet boundary of concentration .....	66
Figure 6.19. Growth rate vs applied potentials for Dirichlet boundary of concentration .....	67
Figure 6.20. Thickness vs time for different fluxes at 0.1V .....	69
Figure 6.21. Thickness vs time for different fluxes at 0.2V .....	69
Figure 6.22. Thickness vs time for different fluxes at 0.3V .....	70
Figure 6.23. Thickness vs time for different voltages at 0.01 mol/m <sup>2</sup> s flux .....	70
Figure 6.24. Thickness vs time for different voltages at 0.05 mol/m <sup>2</sup> s flux .....	71
Figure 6.25. Thickness vs time for different voltages at 0.1 mol/m <sup>2</sup> s flux .....	71
Figure 6.26. Single seed on the anode surface .....	78
Figure 6.27. Anisotropic concentration profiles for t=0s and t=0.05s (top) and t=0.1s and t=0.19s (bottom) for zero flux of concentration and $\phi=0.3V$ .....	80
Figure 6.28. Anisotropic potential profiles for t=0s and t=0.05s (top) and t=0.1s and t=0.19s (bottom) for zero flux of concentration and $\phi=0.3V$ .....	80

Figure 6.29. Snapshot of phase parameter (top), $\text{Li}^+$ concentration (middle) and electric potential (bottom) profiles.....	81
--	----

**LIST OF TABLES**

	Page
Table 2.1. Physical Properties of Cyclic Organic Solvents .....	16
Table 2.2. Physical Properties of Non-Cyclic (Chain) Organic Solvents.....	16
Table 5.1 Values of Parameters used in the Simulations.....	46
Table 5.2 Values of Constants used in the Simulations.....	47
Table 6.1. Properties of different mesh sizes.....	51
Table 6.2. Growth thickness for different values of applied voltage and flux of concentration.....	72
Table 6.3. Comparison of growth thicknesses by using different forms of charge conservation equation for different boundary conditions and 0.1V applied voltage.....	75
Table 6.4. Comparison of growth thicknesses by using different forms of charge conservation equation for different boundary conditions and 0.2V applied voltage.....	76
Table 6.5. Comparison of growth thicknesses by using different forms of charge conservation equation for different boundary conditions and 0.3V applied voltage.....	76

# 1. LITHIUM BATTERIES

## 1.1. BACKGROUND

Fossil fuels play a major role in today's world economy since automobiles, trains, airplanes and a majority of the power plants use oil, natural gas or coal for their fuel. The continued demand for fossil fuels and their depletion leads to serious problems like environmental pollution, environmental change and economic dependence on other nations. Renewable energy sources like wind energy, solar energy, geothermal energy and hydroelectric energy alleviate this problem to a certain extent but they are not capable of generating large quantities of electricity required to run the aforementioned applications and their supply can be unpredictable and inconsistent. Hence, there is a need to develop new technologies which are consistent, have high energy density while having almost negligible effects on the environment. Different battery technologies have emerged to answer the problems of renewable and non-renewable energy sources as they can store and release energy on demand and significant strides have been made in the field of lithium battery technology.

Lithium batteries are the primary sources of power in modern day applications, such as in portable consumer electronics, hybrid electric vehicles (HEVs), implantable electronic medical devices or space vehicles [1-6]. Lithium is the first choice of metals for batteries in modern-day applications because it possesses many key attributes of an energy storage device. Lithium is the lightest metal (density =  $534 \text{ kg/m}^3$ ), high energy density (theoretically  $3860 \text{ mAh/g}$ ), highest standard reduction potential ( $-3.04 \text{ V vs. S.H.E}$ ), no memory effect (i.e. the battery does not have to be completely discharged to be charged again), high volumetric and gravimetric energy densities, good cyclability and low self-

discharge when not in use enable its use as a battery with large specific energy. Figure 1.1. Comparison of different battery technologies in terms of energy densities [4] shows the comparison of different battery technologies, from which it can be observed that lithium battery technologies provide the highest energy density to weight ratios.

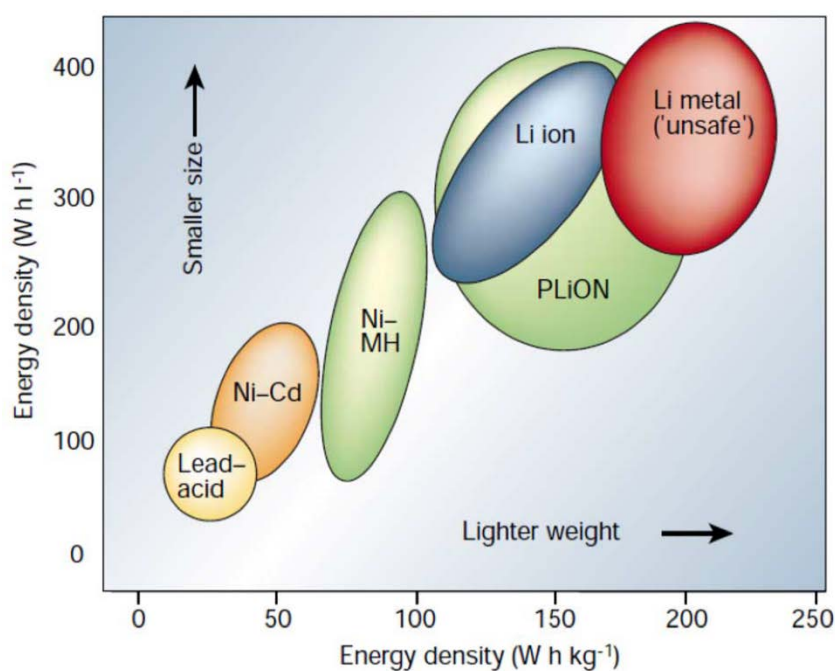


Figure 1.1. Comparison of different battery technologies in terms of energy densities [4]

## 1.2. CURRENT STATE OF THE ART IN LITHIUM BATTERY RESEARCH

Though the commercial production of lithium batteries began only two decades ago, the potential of lithium as an energy source had been identified well over a century

back. The experimentation on lithium batteries began as early as 1912 under Gilbert N. Lewis, who first set up a lithium cell consisting of a pure Li metal anode, a lithium amalgam cathode and an electrolyte of propyl amine saturated with lithium iodide, with its operation carried out in vacuum. The normal electrode potential was found to be 3.3044 V, when compared to other alkali metals, sodium (2.9981 V) and potassium (3.2084 V) [7].

Since the standard reduction potential of lithium is less than -3V, it is highly unstable in protic solvents i.e. solvents displaying hydrogen bonding, such as water. Hence, the realization of practical lithium cells had to await the development of appropriate non-aqueous electrolytes. Subsequently, it was only in the 1950s and 1960s that it was observed that Li-metal was stable in non-aqueous electrolytes such as fused salts, liquid SO<sub>2</sub> or lithium perchlorate (LiClO<sub>4</sub>) in organic solvents. One of the earliest known work on organic electrolytes in lithium batteries came from the PhD thesis of W. Harris, *Electrochemistry in Cyclic Esters*, at University of California, Berkeley. Most of the work during this period was in the form of patent literature, primarily funded by government organizations like NASA and the Department of Defense (DOD) and these patents have been reviewed by Jasinski [8], in which he highlighted the importance of using organic electrolytes in lithium batteries.

Commercialization of primary (non-rechargeable) lithium batteries began in the late 1960s following this discovery. Many such primary lithium batteries include Li/SO<sub>2</sub>, Li/MnO<sub>2</sub>, etc. which are still being manufactured today. These primary, non-rechargeable, batteries are used in watches, calculators and medical implants, to name a few. Li/MnO<sub>2</sub> is the most manufactured primary lithium battery and constitutes roughly about 80% of the lithium battery market [9]. The reasons for this are that these batteries are useful for low-



cost, long-life applications and can operate over a wide range of temperatures ( $-30^{\circ}\text{C}$  to  $60^{\circ}\text{C}$ ).

In 1972, Whittingham at Exxon used a lithium cell with a metallic lithium anode, titanium disulphide ( $\text{TiS}_2$ ) cathode and lithium perchlorate ( $\text{LiClO}_4$ ) in dioxalane as the electrolyte.  $\text{TiS}_2$  was the best intercalation compound available at the time because of its favorable layered structure. Although the cathode worked flawlessly and the cell showed increased cycling efficiency, the shortcomings at the lithium anode/electrolyte interface became rather evident. Microstructure growth of Li metal was observed during each charge-discharge cycle of operation, which led to short circuit and fire hazards [10]. One of the most significant breakthroughs in the research of primary lithium batteries during the 1970s upto the mid-1980s was the discovery of a passivating film on lithium metal when it came in contact with the organic solvents, which was the main reason for stability of these batteries. The success of primary cells based on organic solvents with insoluble ( $\text{SOCl}_2$  or  $\text{SO}_2\text{Cl}_2$ ) and soluble ( $\text{SO}_2$ ) cathodes, especially their long shelf-lives at elevated temperatures are entirely due to this film [11]. It was first Peled [12] who coined the term 'solid electrolyte interface' (SEI) and highlighted that the rate determining step was actually the migration of lithium ions through this interface, rather than charge migration which was previously assumed.

To overcome the issue of microstructure growth and explosions, alternate approaches involving the modification of the negative electrode were followed. This involved using an intercalated compound at the negative electrode as well, as shown in Figure 1.2. Due to the presence of Li in ionic rather than metallic state, the problem of microstructure growth was solved to a large extent, thereby making these Li ion cells much

safer than Li metal cells. This was the next step in the progress of lithium batteries and they were called secondary (rechargeable) lithium batteries. These were lithium batteries which could be recharged after draining all the stored energy. In 1980, John Goodenough et al. proposed the idea of a battery with an intercalated lithium anode and cobalt oxide as the cathode material [13]. To compensate for the increase in potential of the negative electrode, high-potential insertion compounds are needed for the positive electrode, and emphasis shifted from the layered-type transition-metal disulphides to layered or three-dimensional-type transition-metal oxides [14]. Metal oxides are more oxidizing than disulphides (for example, they have a higher insertion potential) owing to the more pronounced ionic character of 'M-O' bonds compared with 'M-S' bonds [15]. Though it took over ten years to implement this concept, this  $\text{LiCoO}_2$  battery created a revolution in the electronics industry, with SONY first commercializing this battery in 1991. These are the Li-ion batteries. They can undergo 400 – 1200 cycles of charge-discharge before slow deterioration of the battery. Theoretically, the primary lithium metal battery can store almost 10 times the amount of energy stored in a conventional lithium-ion battery [16]. This can be attributed to the metallic Li anode in primary lithium batteries. These lithium ion batteries exhibit the same characteristics exhibited by lithium metal batteries, except for the fact that they have a higher safety when compared to lithium metal batteries, as observed in Figure 1.2. Dendrite growth on the anode surface of Li metal battery (top) and Li-ion battery (bottom)[4], which makes it a very popular source of energy in many modern-day applications.

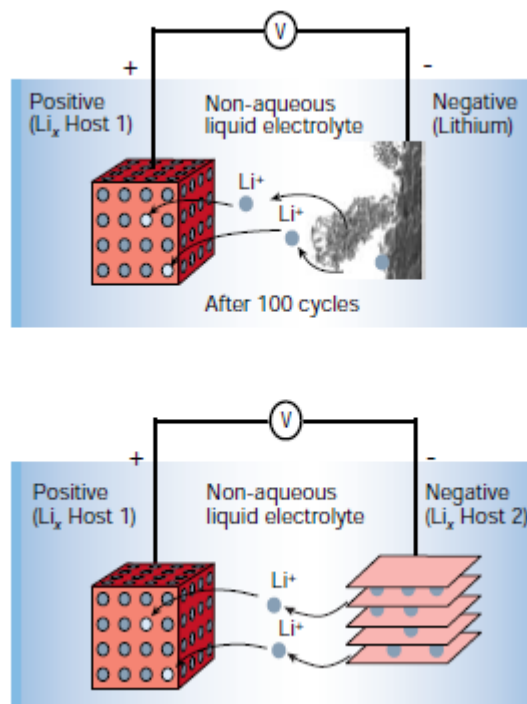


Figure 1.2. Dendrite growth on the anode surface of Li metal battery (top) and Li-ion battery (bottom)[4]

Both lithium-ion batteries (LIBs) and lithium metal batteries (LMBs) consist of the same arrangement – an anode and a cathode, separated by an electrolyte. The major difference between the two is the material of the anode. Lithium metal batteries use pure Li metal as the anode material, while lithium-ion batteries use an intercalated compound of lithium as the anode material i.e. a compound of lithium and graphite (a carbonaceous anode). The electrolyte used in both batteries is a Li salt in a binary organic solvent. The selection of electrolyte salts and solvents for LIBs and LMBs will be made in the next chapter. The cathode can generally be represented as  $\text{Li}_x(\text{MO}_2)_y$ , where M is a transition metal and the most commonly used ones are cobalt (Co), manganese (Mn), nickel (Ni) and vanadium (V).

### 1.3. CURRENT STATUS AND FUTURE PROSPECTS

Secondary lithium batteries rule the market in terms of its applications. Even if the Li-ion battery technology is completely developed, its low energy density cannot meet the demands of the key markets such as automotive and aerospace, in the long term. This factor is propelling the focus of research in lithium battery technology away from conventional Li-ion batteries, in search of a viable alternative which satisfies both criteria of having high energy density as well as having similar safety levels as Li-ion batteries. However, devising Li battery technologies that answer all the shortcomings of the presently used Li battery technologies is a great challenge and would require scientists to explore newer materials and newer electrochemistry. Research conducted over the last few years has yielded the solution to this problem in terms of two new rechargeable Li battery technologies – the Li/air (Li-O<sub>2</sub>) battery and the Li-S battery. These technologies are still rudimentary and there are many challenges to be overcome before they can be commercially produced.

**1.3.1. Lithium Sulfur Batteries.** Sulfur is inexpensive and one of the most abundant elements found on the earth. It can accept up to 2 electrons per atom at ~2.1 V vs Li/Li<sup>+</sup>. Therefore, sulfur cathode materials have a high theoretical capacity of 1675 mAh/g and Li-S batteries have an energy density of around 2600 Wh/kg [17], which is about 6 times higher than the conventional Li-ion battery.

Though this technology sounds promising theoretically, there are many problems with its commercial implementation. On the sulfur cathode side, both the charge product (sulfur) and the discharge product (lithium sulfide) are insulating in nature, resulting in poor material utilization. During cycling, they form a series of long chain lithium polysulfide species which dissolve into the electrolyte, leading to continual loss of active material and rapid capacity decay [18]. Sulfur undergoes a large volumetric expansion of

about 80% upon full lithiation to lithium sulfide, which causes structural damage at the anode [19]. On the anode, along with dendrite growth, the long chain lithium polysulfides (PS) that dissolve into the electrolyte can diffuse to the lithium anode and become reduced to form short chain PS on the surface, resulting in low Coulombic efficiency, which is a major issue in Li-S batteries [19].

**1.3.2. Lithium Air Batteries.** Li-air batteries are those with Li metal anode and an air cathode, which constantly extracts oxygen from the ambient air. The theoretical energy density is around 5200 Wh/kg. Since oxygen is constantly drawn from air, the specific energy should include the oxygen content. This theoretical specific energy is calculated to be 11140 Wh/kg including oxygen, or equivalently 40.1 MJ/kg, which is comparable to that of gasoline, 46 MJ/kg [20, 21].

During their operation, as oxygen is extracted from ambient air, the moisture content in air is also transported into the battery and reacts with the lithium anode. Lithium oxides form during discharge cycle and are transferred to the cathode, where they react with incoming oxygen. These lithium oxides clogs the entire volume of the cathode and prevents transport of both lithium ions and oxygen molecules, hence not preventing it from participating in reversible reactions [22]. This reduces its efficiency and lifespan. The commercial difficulties in implementation is due to difficulties in achieving multiple discharge cycles without losing capacity [23]. Although these batteries provide promising prospects for the future of lithium battery technology, various limitations exist and remain as major hurdles for their transition from a prospect to a commercial technology.

#### 1.4. SAFETY ISSUES

Since the commercialization of the lithium-ion battery by SONY, primary lithium and lithium-ion batteries have become the first choice power sources for consumer electronics, aerospace, military, automotive applications to name a few. Although the energy density of lithium cells is two times higher compared to nickel based cells and four times that of lead acid cells, they come with certain limitations as well. The batteries developed in the 1970s and 1980s were predominantly primary lithium batteries, which offer very high energy densities. All the attempts to commercialize lithium metal batteries during this time period have been unsuccessful, largely because of the poor cycling efficiency and safety issues caused by Li electrodeposits that form on the Li metal anode during the charging process [24]. The behavior of Li metal within a cell can pose hazards as the surface of the negative electrode changes with cycling, forming dendrites that penetrate the separator. Li ions keep accumulating on these dendrites, causing them to grow. As the dendrites grow, there is a strong likelihood that they will come in contact with the surface of the cathode, thereby causing short circuits, as shown in Figure 1.3. Short circuiting in lithium cells [25]. Another safety issue arises from dead lithium. These are structures which have become electrically isolated from the anode surface due to non-uniform dissolution rates of the dendrite microstructure. Their high chemical reactivity can result in short circuits, thermal runaway and eventually fire hazards. Due to these inherent risks posed by primary lithium batteries, a lot of the research shifted towards batteries using lithium ions. Though the lithium ion batteries have lower energy density compared to the lithium metal batteries, they offer a higher safety and provide certain precautions during the charging and discharging process. Despite the high safety standards used during

manufacture of lithium batteries, there have been several reported incidents, which raise the question of safety of this technology and this has raised a large interest among the public in recent years. Since long battery runtimes and more stored energy are ideal in many applications, research has continued in the field of lithium metal batteries.

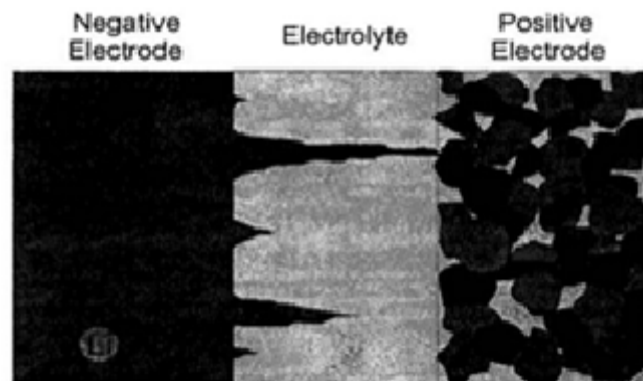


Figure 1.3. Short circuiting in lithium cells [25]

Lithium batteries can provide high currents and discharge rapidly when short-circuited. Although this is beneficial in application that require high currents, a rapid discharge of the battery can lead to overheating of the battery and consequently, fire hazards. To overcome this issue and prevent the possibility of explosions, consumer batteries incorporate either vents, overcurrent or thermal protection.

## 1.5. APPLICATIONS OF LITHIUM BATTERIES

High energy density, low weight and long cycle life have enabled the use of lithium batteries in many modern day applications. These applications, to name a few, encompass both primary and secondary lithium battery technologies –

- Implantable medical devices (Pacemakers)
- Portable electronics (laptops, cell phones, digital cameras, watches etc.)
- Hybrid electric vehicles (Toyota Prius, Chevrolet Volt, BMW i8, etc.)
- Fully electric vehicles (Tesla cars, Nissan Leaf, etc.)
- Space Vehicles (Mars Opportunity rover, etc.)
- Unmanned aerial vehicles (UAVs)
- Satellites
- Weapons systems (Ballistic missiles, etc.)
- Oceanographic instrumentation

Though lithium batteries serve a plethora of applications, not all of them can be beneficial to society. Lithium batteries provide a convenient source of lithium metal, which is used as a reducing agent in the production of methamphetamine. From 2003 to 2014, Missouri was infamously known as the ‘Meth Capital of the World’ because it had the most meth lab raids and busts. Many attempts were made to curb this issue and in 2004, Walmart was even told to limit the sale of lithium battery packages to three in Missouri and four in other states.



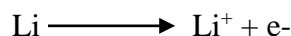
## **1.6. SUMMARY**

This chapter highlights the importance of lithium as an energy source in not only today's world, but also in the future. Efforts are continuously being made to increase the operating safety levels in these batteries. Research has also begun beyond Li-sulphur and Li-air batteries. The incorporation of silicon and germanium nanowires at the electrode surface to reduce this electrodeposition formation is one of them. However, the biggest challenge is reducing the trade-off between energy density and safety levels.

## 2. COMPONENTS OF THE LITHIUM BATTERY

### 2.1. ELECTROLYTES

Electrolytes are vital constituents of electrochemical devices. Electrolyte is a substance which ionizes when dissolved in suitable ionizing solvents. The majority of electrolytes consist of salts dissolved in either an aqueous (water) or non-aqueous (organic solvents) media. When voltage is passed through the electrolyte, the ions diffuse from one electrode to another through the electrolyte, thereby converting chemical energy to electrical energy. In a typical lithium rechargeable battery, during the charging process, the electrons flow from the cathode to the anode externally, whereas the  $\text{Li}^+$  ions flow through the electrolyte. During the charging process,  $\text{Li}^+$  ions move from cathode to the anode and in the opposite direction during the discharge process.  $\text{Li}^+$  ions and electrons are generated from the following chemical reaction:



The selection of the electrolyte in lithium batteries is a complicated task since it has to comply with many contrasting requirements such as high conductivity, high transference number, good chemical and thermal stability, low viscosity and toxicity, good dielectric constant, ability to form a stable solid electrolyte interface (SEI), should remain a liquid over a wide temperature range, commercially inexpensive and readily available [26-29].

Since an 'ideal solvent' is yet to be found (high dielectric constant and low viscosity), practical lithium batteries use mixed solvents i.e. a main solvent with high dielectric constant and viscosity and a secondary solvent with low values of dielectric constant and viscosity. Many lithium salts and organic solvents have been identified as electrolytes for lithium batteries. Some common lithium salts are lithium perchlorate

(LiClO<sub>4</sub>), lithium tetrafluoroborate (LiBF<sub>4</sub>), lithium hexafluorophosphate (LiPF<sub>6</sub>) and lithium bis (trifluoromethanesulfonyl)mide (LiTFSI). The organic solvents used are ethylene carbonate (EC), propylene carbonate (PC), ethyl methyl carbonate (EMC), dimethyl carbonate (DMC) and diethyl carbonate (DEC). From various studies conducted on selection of electrolyte for lithium batteries, it has been found that LiPF<sub>6</sub> in binary organic mixture of a cyclic (EC) and non-cyclic (DMC) organic compounds satisfies (all the aforementioned properties of the required electrolyte [30, 31].

In this study, the system consists of an anode made of pure lithium, a cathode made of LiCoO<sub>2</sub>, separated by LiPF<sub>6</sub> electrolyte, mixed in a 1:1 ratio of ethylene carbonate (EC) and dimethyl carbonate (DMC).

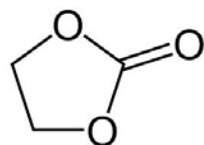
It has been predicted theoretically [32], and several authors have reported that, when depositing a metal from a binary electrolyte, dendritic growth starts when the concentration of metal ions approaches 0 at the negative electrode [33].

**2.1.1. Organic Solvents.** The organic solvent should be a polar solvent not having an active proton because the material for the organic electrolyte coexists with the anode and cathode materials within the cell. The ideal solvents used in lithium batteries must meet the following minimum requirements [34]:

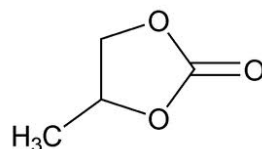
- They must be able to dissolve sufficient amounts of lithium salt concentration i.e. they should have a high dielectric constant
- They should have low viscosity to facilitate ion transfer
- They should remain inert towards materials of cell components i.e. anode, cathode, separator and cell packaging materials

- They should remain liquid over a wide temperature range i.e. it must have a low melting point and high boiling point
- They should be non-toxic and economical.

Cyclic organic solvents have high viscosity and high dielectric constant. Non-cyclic organic solvents have low viscosity and low dielectric constant. Hence, a mixture of these two types of organic solvents would produce the desired properties of solvent in lithium batteries i.e. low viscosity and high dielectric constant. Figure 2.1 and Figure 2.2 represent the ring and chain structures respectively, of different organic compounds. Table 2.1 and Table 2.2 show the physical properties of the different organic compounds that can be used in commercial lithium batteries as solvents and the differences in properties between them can be seen.



(a)



(b)

Figure 2.1. Ring structures of cyclic organic compounds used in lithium batteries  
(a) Ethylene carbonate - EC and (b) Propylene carbonate - PC

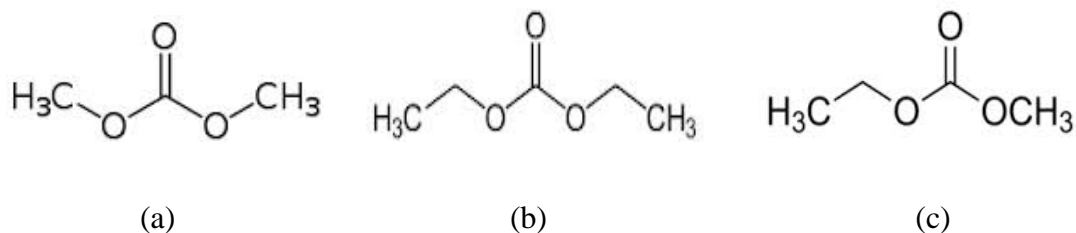


Figure 2.2. Chain structures of non-cyclic (linear) organic solvents used in lithium batteries (a) Dimethyl carbonate - DMC (b) Diethyl carbonate – DEC and (c) Ethyl Methyl carbonate - EMC

Table 2.1. Physical Properties of Cyclic Organic Solvents

Polymer	Melting point (°C)	Boiling point (°C)	Viscosity (Pas)	Density (g/mL)	Vapor pressure (mmHg)	Dielectric constant	Dipole moment (D)
Ethylene carbonate (EC) – $C_3H_4O_3$	35-38	260.7	0.480	1.321	0.02	90	5.68
Propylene carbonate (PC) – $C_4H_6O_3$	-48.8	241.7	0.0025	1.2006	0.045	64.9	4.54

Table 2.2. Physical Properties of Non-Cyclic (Chain) Organic Solvents

Polymer	Melting point (°C)	Boiling point (°C)	Viscosity (Pas)	Density (g/mL)	Vapor pressure (mmHg)	Dielectric constant	Dipole moment (D)
Dimethyl carbonate (DMC) – $C_3H_6O_3$	2-4	90	0.000625	1.069	18	3	0.76

Table 2.2. Physical Properties of Non-Cyclic (Chain) Organic Solvents (contd.)

Diethyl carbonate (DEC) – $C_5H_{10}O_3$	-43	126-128	0.000749	0.9752	10.8	2.82	0.96
Ethyl methyl carbonate (EMC) – $C_4H_8O_3$	-53	107	0.00065	1.01	14.7	2.95	0.89

**2.1.2. Lithium Salts.** The solute selected for the electrolyte in lithium batteries must ideally meet the following requirements [34]:

- It should be able to completely dissolve in the non-aqueous media and the  $Li^+$  cation must be able to move around with high mobility
- The anion must be stable against oxidative decomposition
- The anion should be inert towards the organic solvents
- The anion must be non-toxic and thermally stable against chemical reactions that occur
- The anion and cation must remain inert towards other materials in the cell such as separator, cell packaging materials and electrode surfaces.

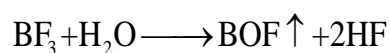
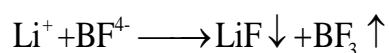
Aravindan et al [35] presented the following advantages and limitations of using certain lithium salts:

**2.1.2.1. Lithium perchlorate (LiClO<sub>4</sub>).** LiClO<sub>4</sub> is very acidic in nature, has high ionic conductivity in non-aqueous solvents, high solubility and high anodic stability. It is strongly involved in the solid electrolyte interface (SEI) formation and exhibits an ionic conductivity of 9 mS/cm in EC/DMC at room temperature [36]. The high oxidation state of chlorine makes it a strong oxidizing agent, which readily reacts with organic solvents at higher temperatures potentially leading to explosions.



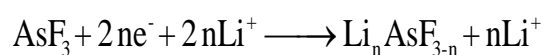
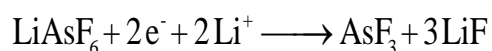
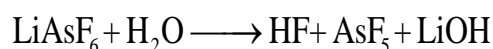
The by-product of this reaction, LiClO<sub>3</sub>, is hygroscopic in nature i.e. it absorbs the moisture and leads to explosions during cycling of the battery. Hence, it cannot be used in practical lithium batteries.

**2.1.2.2. Lithium tetrafluoroborate (LiBF<sub>4</sub>).** LiBF<sub>4</sub> exhibits high solubility in non-polar solvents. It has greater thermal stability and exhibits greater moisture tolerance when compared to that of LiPF<sub>6</sub> [37] However, it shows only a moderate ionic conductivity of 4.9 mS/cm. LiBF<sub>4</sub> absorbs even with trace amounts (in ppm level) of moisture and undergoes hydrolysis to form hydrogen fluoride (HF), which can destroy the d-block metal present in the cathode as well as the Li<sup>+</sup> ion. The BF<sub>4</sub><sup>-</sup> ion is too stable and cannot participate in the formation of a stable SEI.



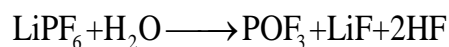
These disadvantages make LiBF<sub>4</sub> unsafe to use in practical lithium batteries, but they are extensively used in testing of lithium secondary batteries.

**2.1.2.3. Lithium hexafluoroarsenate (LiAsF<sub>6</sub>).** LiAsF<sub>6</sub> has a very high ionic conductivity of 11.1 mS/cm [38]. It is soluble in low dielectric constant solvents i.e. non-cyclic organic solvents in lithium batteries, and its average cycling efficiency is found to be greater than 95%. The anodic stability of LiAsF<sub>6</sub> is very high, 6.3 V vs Li/Li<sup>+</sup> and 4.5 V at the cathode. Although LiAsF<sub>6</sub> has so many desirable properties, its toxicity is the major concern in implementation and hence, this salt has never been used in any commercial battery. Moisture is again an issue with LiAsF<sub>6</sub> as it produces HF during chemical reaction.



The strong nature of the AsF<sub>6</sub><sup>-</sup> ion results in decomposition of the salt. The by-products of reaction HF, AsF<sub>5</sub> and AsF<sub>3</sub> can react with the SEI and break it.

**2.1.2.4. Lithium hexafluorophosphate (LiPF<sub>6</sub>).** This is the most widely used lithium salt in lithium batteries since it satisfies most of the desired qualities of a salt. It has good ionic conductivity of 10.7 mS/cm. It is highly soluble in low dielectric media. Its thermal and anodic stabilities are comparable to most other lithium salts used in lithium batteries. It forms a stable solid electrolyte interface (SEI). At elevated temperatures, operation with LiPF<sub>6</sub> is a problem due to its poor thermal stability. LiPF<sub>6</sub> absorbs even trace amounts (in ppm level) of moisture present in the electrolyte and undergoes hydrolysis to form dangerous products like HF.





**2.1.2.5. Lithium bis (trifluoromethanesulfonyl) mide – Li[N(CF<sub>3</sub>SO<sub>2</sub>)<sub>2</sub>] or LiTFSI.** LiTFSI is thermally stable at its melting temperature of 236<sup>0</sup>C and does not decompose until 360<sup>0</sup>C. It has a slightly lower conductivity when compared to LiPF<sub>6</sub> and LiAsF<sub>6</sub>. It dissociates well in lower dielectric constant media. Hence, solution viscosity increases and mobility tends to decrease, favoring higher ionic conductivity. The oxidation potential of LiTFSI is found to be 4.3V vs Li/Li<sup>+</sup> and this value is very high compared to other salts, apart from LiAsF<sub>6</sub>. Though LiTFSI has so many desirable properties, it has not been used in any commercial battery because of corrosion problems.

A comparison of properties among the aforementioned lithium salts is shown below -

Dissociation constant - LiBF<sub>4</sub> < LiClO<sub>4</sub> < LiPF<sub>6</sub> < LiAsF<sub>6</sub> < LiTFSI

Average ion mobility - LiBF<sub>4</sub> > LiClO<sub>4</sub> > LiPF<sub>6</sub> > LiAsF<sub>6</sub> > LiTFSI

Anodic stability – ClO<sub>4</sub><sup>-</sup> < BF<sub>4</sub><sup>-</sup> < PF<sub>6</sub><sup>-</sup> < AsF<sub>6</sub><sup>-</sup>

## 2.2. SOLID ELECTROLYTE INTERFACE (SEI)

It is well known that cyclic life and stability of lithium batteries are dependent on the formation of an organic/inorganic layer at the electrode face, called the solid electrolyte interface (SEI). According to Peled [12], the SEI must have the following properties – the electron transference number must be zero, high ion conductivity, uniform morphology and chemical composition for homogeneous current distribution, good adhesion to the anode surface, good mechanical strength and flexibility and low solubility in electrolytes.

The SEI prevents anode lattice structure from exfoliation of atoms on the anode surface and allows charging of battery without major capacity fades [39]. The SEI film formation differs significantly among the various organic solvents. For example, the SEI

film is formed in ethylene carbonate (EC) based electrolyte, whereas SEI film is not formed in propylene carbonate (PC), unless it has an additive like vinylene carbonate (VC) added to it. The SEI formation depends on a number of factors like reactivity of the solvent, physical properties of the film, interaction of the film with the electrode surface, taking the same lithium salt. It has been reported that EC gets decomposed in a battery electrolyte of EC/DMC and that DMC mainly contributes in improving the viscosity and conductivity [40]. On repeated charge/discharge cycles, the SEI breaks down and formation of dendrites takes place in those areas. It has been reported through an in situ spectroscopic ellipsometry study that the average thickness of the SEI layer is ~27 nm [41].

### **2.3. ELECTRODES**

As mentioned earlier, any battery system consists of three components – an anode, a cathode and an electrolyte. A battery is a transducer which converts chemical energy into electrical energy. The materials to be used for the anode and cathode are instrumental in determining the electric potential difference. The electric potential is measured as a difference between the chemical potentials of lithium in the anode and the cathode and is given by  $\Delta G = -nFE$  (on simplification from the Nernst equation), where  $\Delta G$  is the change in Gibbs free energy,  $n$  is the number of moles of electrons,  $F$  is the Faraday's constant ( $F = 96485.33 \text{ C/mol}$ ) and  $E$  is the cell potential in volts.

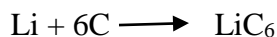
In the case of direct current (DC), electrodes come in pairs – an anode and a cathode. The anode is the electrode at which the electrons leave the cell and oxidation occurs. The cathode is the electrode at which the electrons enter the cell and reduction occurs. In a primary cell, the identities of the electrodes remain fixed. The anode is always

the negative electrode and the cathode is always the positive electrode. Such cells can be discharged but not recharged. However, in secondary cells, the chemical reactions are reversible. When the cell is being charged, the cathode loses electrons and they flow towards these anode. When the cell is being discharged, the secondary cell behaves like a primary cell. Hence, secondary cells are rechargeable. For an overall perspective, only the commonly used electrode materials are presented (both anode and cathode) in the following sections.

**2.3.1. Anode in Lithium Batteries.** The material used in the anode is the major difference between lithium metal batteries and lithium ion batteries. The properties exhibited by these batteries are contingent on the material of the anode. In lithium metal batteries, the anode is made of pure metallic lithium, while it is made of a lithiated compound intercalated with either carbon or silicon ( $\text{Li}_x\text{C}_y$  or  $\text{Li}_x\text{Si}_y$ ) in lithium-ion batteries.

**2.3.1.1. Lithium metal anode.** The research in the field of lithium batteries began with a battery having a pure metallic lithium anode. The main reason for this being that lithium metal batteries are able to provide a very high specific capacity (3860 mAh/g) [42]. Though metallic lithium offers several advantages over intercalated lithium anodes, its main drawback is safety, which prevents its commercial implementation for larger applications.

**2.3.1.2. Intercalated lithium compound anode.** These type of anodes are extensively used in rechargeable lithium batteries i.e. lithium-ion batteries. The anode is made of a lithiated compound intercalated with either carbon or silicon ( $\text{Li}_x\text{C}_y$  or  $\text{Li}_x\text{Si}_y$ ) in lithium-ion batteries. The more extensively used or standard anode materials in lithium-ion batteries are carbonaceous anodes, either graphite or coke. During the charging cycle, the reaction at the anode is:



Lithium-ion batteries provide a significantly smaller specific capacity of 372 mAh/g for graphite anode [43]. The benefit of using anodes are low cost and good energy density. Since graphite can accommodate one lithium atom per 6 carbon atoms, it cannot produce a high energy capacity. To increase the energy capacity i.e. how long a battery can

retain its charge before discharge cycle begins, there have been efforts to replace graphene sheets with Silicon (Si). Si can hold one lithium atom per 4.4 Si atoms, thus producing a higher energy capacity. Despite this advantage, Si contracts and expands erratically during the charging cycle, causing fragmentation and losing its energy capacity rapidly [44]. Though lithium metal batteries produce almost 10 times the capacities produced by lithium-ion batteries, they are not feasible due to onset of failure during the first few cycles of charging itself, whereas lithium-ion batteries only begin failing after 400-1200 cycles of charge, as discussed in the previous chapter.

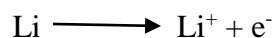
**2.3.2. Cathode in Lithium Batteries.** The choice of material to be used for the cathode depends whether we are dealing with rechargeable lithium metal batteries or Li-ion (secondary) batteries. For the case of lithium metal batteries, owing to the pure metallic nature of the lithium anode, the cathode does not need to be lithiated with any elements/compounds before cell assembly. However, in Li-ion batteries, since there is no lithium in the carbonaceous anode, the cathode must act as a source of Li and it must therefore use a Li based intercalation compound to facilitate cell assembly [45].

For materials to be used as cathodes in lithium batteries, they must meet the following requirements [46]:

- The material must contain a readily reducible or oxidizable ion i.e. a transition metal preferably
- The material must be able to react with lithium in a reversible manner (if it is a rechargeable lithium metal battery)
- High capacity, preferably one Li per transition metal atom, leading to high energy storage

- The material reacts rapidly with lithium on insertion and removal, leading to a high power density
- Must be a good electronic conductor, preferably a metal
- The material must be stable i.e. it must not overcharge or overdischarge
- The material must be economical
- The material should be environmentally benign

The cathode materials in lithium batteries are typically oxides of transition metals and can be generically denoted as  $\text{Li}_x(\text{MO}_2)_y$ , where M is a transition metal like cobalt (Co), manganese (Mn), vanadium (V), nickel (Ni) etc. While oxidation of a transition metal can maintain charge neutrality in the compound, large compositional changes lead to phase changes. Therefore, crystal structures which are stable over a wide composition range must be used. This is a challenge during the charging process when most of the lithium is removed from the cathode. The rates of charging and discharging, control the amount of discharge current. The performance of the cathode depends on movement of lithium ions from electrolyte to the electrode, electrode surface morphology, as well as the inherent electrochemical properties of the cathode material [47]. During charging, the lithium at the cathode dissolves to form lithium ions and free electrons. The reaction at the cathode is represented as:



Fergus [47] mentions the following commonly used cathode materials in lithium batteries today and some of their advantages and limitations:

**2.3.2.1. Lithium cobalt oxide (LiCoO<sub>2</sub>).** This is the most commonly used and commercially produced cathode material in lithium batteries [48]. The first proposed lithium-ion battery by John Goodenough in 1980 was constructed using a LiCoO<sub>2</sub> cathode. However, certain problems associated with LiCoO<sub>2</sub> are that it is quite unstable and can deteriorate when it is overcharged, liberate oxygen into the electrolyte, which can cause a violent reaction when heated above its flash point i.e. they have poor thermal stability [49].

**2.3.2.2. Lithium manganese oxide (LiMn<sub>2</sub>O<sub>4</sub>).** Since manganese (Mn) is inexpensive, these cathodes are suitable in applications which require a long life, but are low cost. They have a relatively high energy density per mass (280 Wh/kg) and per volume (580 Wh/L). This is the most common consumer-grade battery cathode material and forms about 80% of the lithium battery market. When the battery is not in use for long periods, loss of capacity has been observed due to dissolution of manganese in the electrolyte. One method of overcoming this limitation is to add iron (Fe) or cobalt (Co) to LiMn<sub>2</sub>O<sub>4</sub>.

**2.3.2.3. Lithium nickel oxide (LiNiO<sub>2</sub>).** It is lower in cost and has a higher energy density (20% by weight and 15% by volume), but is less stable when compared to LiCoO<sub>2</sub>. It is very similar to LiCoO<sub>2</sub> in structure and has been pursued because of the less availability of cobalt.

**2.3.2.4. Lithium iron phosphate (LiFePO<sub>4</sub>).** These are a class of LiMPO<sub>4</sub> cathodes, where M is a transition metal and this is the most commonly used phosphate cathode. Other phosphates which are used as cathodes in lithium batteries are LiMnPO<sub>4</sub>, LiCoPO<sub>4</sub> and LiV<sub>2</sub>(PO<sub>4</sub>)<sub>3</sub>.

**2.3.2.5. Composite cathodes.** Composite cathodes, as the name suggests, is a combination of two electrode materials to form a new one. This is done to improve performance of a battery during charge and discharge cycles, increase energy retention and improve battery life. For example, addition of  $\text{LiFePO}_4$  to  $\text{LiCoO}_2$  or  $\text{LiNiO}_2$ . Rather than addition of different particles to a particular cathode, composite cathodes can also be prepared by coating an active material to the surface of a cathode material.

## **2.4. SUMMARY**

A detailed description of all the different types of electrolytes and electrodes used in lithium batteries is mentioned. The advantages and disadvantages of using different electrolytes and electrodes can be seen. With these factors in mind, the selection of the most optimum electrolyte and electrode components for a lithium battery for a particular application can be made appropriately.



### **3. COMPUTATIONAL MODELING TECHNIQUES FOR MICROSTRUCTURE EVOLUTION**

#### **3.1. UNDERSTANDING THE EVOLUTION OF MICROSTRUCTURES**

Microstructures are compositional and structural inhomogeneities that arise during processing of materials. Microstructures mainly evolve to lower the free energy of a system and bring the system to a state of equilibrium. These structural features usually have an intermediate mesoscopic length scale in the range of nanometers to microns. The size, shape, and spatial arrangement of the local structural features in a microstructure play a critical role in determining the physical properties and performance of a material [50]. The formation of different microstructures are affected by the processes and the conditions through which they are evolved. In order to develop engineering materials and enable design of newer multifunctional materials, it is essential to predict the microstructural patterns such as size, shape and spacing of observed microstructures in materials. For example, in structural applications where high strength is crucial, the steels contain a mix of refined crystal grains and a dispersion of soft and hard phases throughout their microstructure. In aerospace and automotive applications, where high strength-to-weight ratios are of utmost importance, lighter alloys are strengthened by precipitating second-phase particles in the original grain structure. So, understanding microstructure evolution helps us to understand the properties and behavior of materials and vice-versa.

Microstructures are thermodynamically unstable structures that form in a material that form due to various processing techniques. Their formation is governed by a thermodynamic driving force and this driving force varies as the process varies. For example, processes like solidification and electrodeposition are driven by minimization of free energy, while phase transformation would include elastic effects and driven by

changes in surface energy and anisotropy. There are several experimental methods to observe the transformed morphology in a material like optical microscopy, electron microscopy, X-ray diffraction, to name a few. But there has been a need to observe the growth of microstructures without utilizing too many resources and eliminating the possibilities of human error during experimentation. Hence, the focus of research shifted from studying the growth of these materials experimentally to predicting the growth of these materials computationally. Modeling the formation of these microstructures is important as it gives insight into factors like growth rate and also the effect of different parameters on their evolution. The ability to model and predict the evolution of material microstructures has vastly been due to the invention of better numerical and computing tools. Phase field and sharp interface techniques have made it possible to model free surface kinetics which are responsible for evolution of microstructures [51]. Each computational model is governed by a set of governing partial differential equations and a series of boundary conditions to describe the system under study. These mathematical relations, in theory, contain the physics that leads to evolution of these microstructures. However, each technique is accompanied by its own advantages and limitations.

### **3.2. SHARP INTERFACE MODEL**

In the conventional modeling technique for phase transformations and microstructural evolution i.e. the sharp interface approach, the interfaces between different domains are considered to be infinitely sharp, and a multi-domain structure is described by the position of the interfacial boundaries. The kinetics of microstructure formation is then modeled by a set of partial differential equations that describe the release and diffusion of

heat, the transport of impurities, and the complex boundary conditions that govern the thermodynamics at the interface for each domain. In a sharp-interface model [52], the regions separating the compositional fields are considered as mathematically sharp interfaces so one or more variables and/or their derivatives are typically discontinuous across the interface. Tracking of the interface will be required at each and every step of computation. This method of tracking the interface is simple in one-dimensional studies, but becomes numerically complex and impractical for two-dimensional and three-dimensional cases. Here, the order parameter is a discontinuous function and it only takes 2 values, 0 (liquid phase) and 1 (solid phase) and does not define the phases in between.

### **3.3. PHASE FIELD MODEL**

Compositional and structural inhomogeneities that occur during processing of metals may consist of phases of dissimilar compositions and crystal structures, grains with different orientations or metals with some defects in them. The phase field method has emerged as one of the most versatile techniques to simulate microstructure evolution during many complex phenomena like solidification [53-58], solid state phase transformation [59-61], electrodeposition [62-65], crack propagation [66], dislocation dynamics [67] and various other phenomena.

In the phase field model, the order parameter is a continuous function which transitions smoothly from liquid to solid phase. The order parameter,  $\eta$ , assumes values between 0 (in the liquid phase) and 1 (in the solid phase) respectively. This gives rise to a small interface between them, where the meta-stable phases are described as  $0 < \eta < 1$ , as illustrated in Figure 3.1. This interface is not a physical entity, but a mathematical entity

assumed for convenience of modeling. It assumes constant values in the bulk of each phase, continuously interpolating between its bulk values across this thin boundary/interface. The interface thickness is controlled by surface energy and height of the double well potential function. The concept of a diffuse interface was first analyzed by van der Waals, who examined the density change between a liquid and its vapor [68], who concluded that diffuse interface between stable phases in a material is more natural than the assumption of a sharp interface in the properties of the material.

### **3.4. SHARP INTERFACE MODEL VS. DIFFUSE INTERFACE (PHASE FIELD) MODEL**

A limitation encountered in modeling sharp interface models is that it cannot be used to describe many physical phenomena like effect of mobile dislocations on particle coarsening. A similar situation is encountered when solute trapping is considered.

Another drawback associated with sharp interface models is that their numerical simulation also turns out to be extremely difficult. The most challenging aspect is the complex interactions between topologically complex interfaces that undergo merging and pinch-off during the course of a phase transformation. Such situations are often addressed by applying somewhat arbitrary criteria for describing when interface merging occurs and by manually adjusting the interface topology. The numerical codes for sharp interface models are very lengthy and complex, particularly in three-dimensional systems. The sharp interface model would require two equations to describe the phases and one more to track the interface, whereas phase field models require only a single equation to describe phase transformation. This is mainly because meshing the domain using the finite element method allows easy tracking of the interface.

Along with these two drawbacks of sharp interface models, one would not be able to completely appreciate the diffuse interface approach if the most important advantage of the latter over former is not mentioned here. Main advantage gained by using phase-field method to model phase transitions, compared to the sharp-interface method, is that the explicit tracking of the moving surface, the liquid and solid interface, is completely avoided. Instead, the phase of each point in the simulated volume is computed at each time step. In classical sharp interface formulation, the basic equations have to be written for each medium and the interface boundary conditions must be explicitly tracked. In diffuse-interface theory the basic equations, with supplementary phase field terms, are deduced from a free energy functional for the whole system and interface conditions do not occur. In fact, they are replaced by a partial differential equation for the phase field.

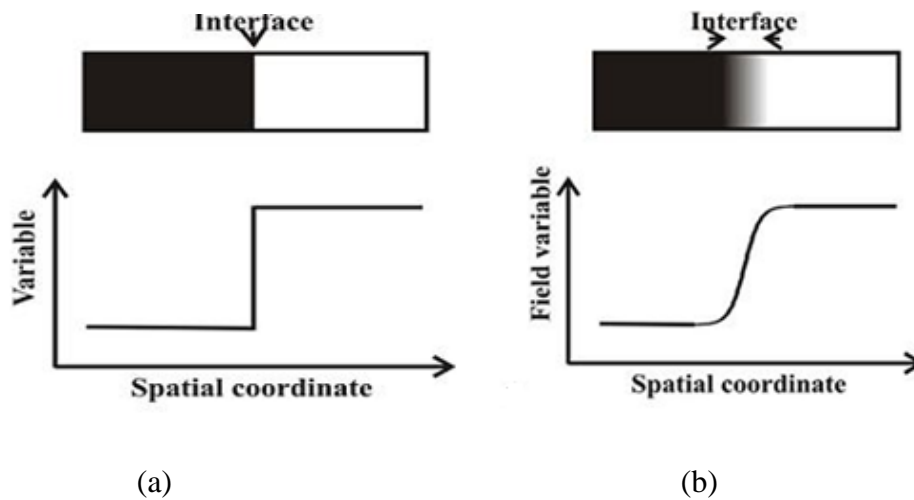


Figure 3.1. Graphical representations of (a) Sharp Interface Model and (b) Diffuse Interface (Phase Field) Model

### **3.5. LIMITATIONS OF PHASE FIELD MODELS**

While phase field models might offer a deeper connection to fundamental thermodynamics than larger-scale engineering or sharp interface models, they come with several problems that have traditionally stood in the way of making models amenable to quantitative modeling of experimentally relevant situations. For example, the emergence of a mesoscopic interface renders phase field equations very stiff. This requires multi-scale numerical methods to resolve both the thin interfaces that are inherent in phase field models while at the same time capturing microstructures on larger (millimeter-centimeter) scales. Moreover, the numerical time steps inherent in phase field theory (limited by the interface kinetics) makes it impossible to model realistic time scale. As a result new mathematical techniques (thin-interface asymptotic analysis methods) have to be developed that make it possible to accelerate numerical time scales without compromising solution quality. Luckily, advances on both these fronts (and others) have recently become possible to overcome some of these challenges in selected problems.

### **3.6. SUMMARY**

Computational modeling holds the edge over experimentation as the first step since it requires lesser resources to predict many different phenomena and understand the parameters controlling them. Using this knowledge, one can conduct experiments to corroborate the results of the simulations. Two modeling techniques – sharp interface modeling and phase field modeling are presented and the differences between them have also been highlighted. Since the focus of this work is phase field modeling, its uses, advantages and limitations over sharp interface modeling have also been made.

#### 4. CURRENT PHASE FIELD MODELS OF ELECTRODEPOSITION PROCESS

The importance of lithium batteries to the energy sector and phase field modeling as a computational tool for predicting microstructures have been made in Chapters 1 and 3 respectively. The growth of microstructures from the anode surface during electrodeposition is not present only in lithium batteries, but is present in every electrochemical system and there have been many phase field modeling studies of the parameters responsible for this phenomenon, through many different methods. Guyer et al. [69, 70] presented a generalized phase field model for aqueous electrochemical systems, which placed emphasis only on the critical details about the thermodynamics of the interface in general and the electrochemical double layer in particular. For this reason, they considered all the components in the system i.e. cations of the metal under consideration, anions and cations of the salt present and electrons produced during the charging process as well. These reasons render this model is extremely complicated for practical purposes and to model macroscopic systems. Shibuta et al. [64] developed a phase field model for the electrodeposition of Cu from  $\text{CuSO}_4$ , where the evolution equations were derived considering a dilute solution approximation, as done in the KKS model [54] and a simplified charge conservation equation (a Laplace's equation). The same group [63] developed another phase field model for the electrodeposition of  $\text{Cu}^{2+}$  ions by considering Butler-Volmer kinetics by applying a non-linear diffusivity term and used the Poisson-Nernst-Planck equation to define the charge conservation equation. While not exactly a phase field model, Akolkar [62] developed a mathematical model for the growth of dendrites in Li batteries. The evolution equation was derived using Fick's second law and the effects of growth of dendrites as a function of tip current density and overpotentials

were studied. This model used a concentration dependent diffusivity term and mainly pointed out that the propagation of the electrodeposits are due to the tip of the initial electrodeposit as its tip is thermodynamically very unstable. Liang et al.[65, 71], using Butler-Volmer kinetics and a time dependent evolution source term for both concentration and electric potential, studied the effects of electrodeposition in a Li-ion battery. They showed the effects of charging density and overpotential on the microstructure growth rate. Cogswell [72] studied the electrodeposition of  $Zn^{2+}$  from  $ZnSO_4$  using Marcus kinetics instead of the traditional Butler-Volmer kinetics. Transfer of a charge species can be modeled in two ways – the phenomenological, macroscopic Butler-Volmer model and the microscopic Marcus-Hush model [73]. The Butler-Volmer method offers a simple way to model electrochemical systems while the Marcus model concentrates more on the kinetics at the electrode of different species, while trying to maintain computational simplicity of modeling macroscopic systems.

The aspects of phase field modeling that will be used are discussed below, first in a generalized form and those aspects will then be applied to derive the governing equations for the present model.

#### **4.1. PHASE FIELDS AND THEIR EVOLUTIONS**

The phase field variable distinguishes between different states of a material that may be identical in all other state variables such as temperature, concentration, pressure, etc. Therefore, the phase-field variable is an independent state variable. In their theory of phase transitions, Ginzburg and Landau used this observation to expand the thermodynamic state functions, which they called ‘order parameter, shown in Figure 4.1.



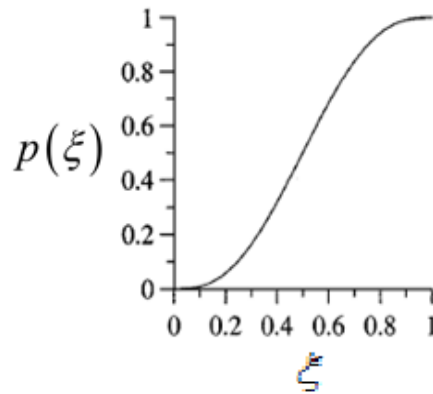


Figure 4.1. Variation of order parameter interpolating function  $p(\xi)$  [52]

In a two-phase system, the order parameter,  $\eta$ , assumes values of 0 and 1 in the phases respectively, as shown in Figure 4.1. In general, for an N-phase system, the value of order parameter at any point in the system can be represented as

$$\sum_{i=1}^N \eta_i = 1$$

The order parameter defines the state of phase of a system during phase transformation. In other words, it describes the change of symmetry from a disordered phase to an ordered phase. For example, a crystal has fewer rotational and translational symmetries compared to a liquid. The order parameter takes on a finite value in the ordered state but vanishes completely in the disordered state. But for some phase changes, like vapor to vapor + liquid, there is no change in the structural symmetry groups of the parent and daughter phases. In such cases, effective order parameters can often be defined in terms of density differences relative to the parent phase.

The order parameter may be of two types – conserved and non-conserved. Conserved order parameters are order parameters whose value does not change during a phase transformation. Non-conserved order parameters are those whose value changes during the course of a phase transformation.

**4.1.1. Conserved Order Parameter.** Conserved order parameters are order parameters whose values do not change during a phase transformation. From the Ginzburg-Landau theory, a local chemical potential must be derived as a functional of concentration. A description of the free energy functional will be made in the coming sections. If  $F$  represents the free energy functional and  $C$  represents the concentration, then the chemical potential can be represented as a variational derivative as

$$\mu = \frac{\delta F}{\delta C} \quad (1)$$

In the equilibrium state, the chemical potentials of the two phases will be equal to each other. Since concentration,  $C$ , is a conserved field, it must satisfy the mass conservation equation

$$\frac{\partial C}{\partial t} = -\nabla \cdot \vec{J} \quad (2)$$

The flux is defined as

$$\vec{J} = -M\nabla \mu \quad (3)$$

where  $M$  is the diffusional mobility. By combining equations (2) and (3), we obtain the following equation of motion for the concentration field

$$\frac{\partial C}{\partial t} = \nabla \cdot \left( M\nabla \frac{\delta F}{\delta C} \right) \quad (4)$$

This is the Cahn-Hilliard equation which represents the mass conservation equation and this equation is used to derive the governing equation for concentration in this work.

**4.1.2. Non-Conserved Order Parameter.** Non-conserved order parameters are those whose value changes during the course of a phase transformation. In an irreversible process, to satisfy the equilibrium condition, the dissipation of free energy vs. time must follow the inequality

$$\frac{\delta F}{\delta t} \leq 0 \quad (5)$$

The driving force for the rate of change of non-conserved order parameter is defined as

$\frac{\delta F}{\delta \eta}$ , where  $\eta$  represents the phase field order parameter.

Since there is no conservation imposed on  $\xi$ , the dynamic evolution of non-conserved order parameter is given by

$$\frac{\partial \eta}{\partial t} = -L_p \frac{\delta F}{\delta \eta} \quad (6)$$

(6) is the Allen-Cahn equation, where  $L_p$  is the phase field mobility. This equation is used to derive the governing equation for phase field order parameter if the free energy density is a function of order parameter as well. Though this equation has not been used in this work, it has to be noted that if a free energy density function is formulated such that it is a function of both order parameter and concentration, then the governing equation for the phase field order is derived using the Allen-Cahn equation.

**4.1.3. The Ginzburg-Landau Free Energy Functional.** The Ginzburg-Landau free energy functional,  $F$ , forms the base of the work of this thesis. It is a combination of chemical free energy density and gradient free energy of the system. The state of a system can be represented by the order parameter,  $\eta$ , in the phase field model. The entire phase field can be represented as:  $\eta=1$  represents the electrode and  $\eta=0$  represents the electrolyte and  $0 < \eta < 1$  represents the interface between these two phases. The changes in time of the phase field and concentration of  $\text{Li}^+$  ions are assumed to be proportional to the variation of the Ginzburg-Landau free energy functional. In all other phase field models for electrodeposition [64, 65, 69, 71, 72], the functional,  $F_c$ , which is a function of both order parameter,  $\eta$ , and molar concentration,  $C$ , is defined as:

$$F_c = \int_v \left( f(\eta, C) + \frac{1}{2}k(\nabla\eta)^2 + \rho\phi \right) dV \quad (7)$$

where the  $f(\eta, C)$  is the chemical free energy density,  $k$  is the coefficient of gradient energy,  $\rho$  is the electrical charge density and  $\phi$  is the electric potential.

## 5. PROPOSED PHASE FIELD MODEL FOR ELECTRODEPOSITION IN LITHIUM METAL BATTERIES

### 5.1. PROPOSED PHASE FIELD MODEL

The definition of free energy for a system depends on the thermodynamic state of that system. Entropy is appropriate for a system which is not isothermal, Gibbs free energy is appropriate for an isothermal system at constant pressure, and Helmholtz free energy is appropriate when temperature and volume are kept constant [74]. In this work, Gibbs free energy is utilized. The free energy density functions defined in all other phase field models for electrodeposition [64, 69, 72] are a function of both order parameter,  $\eta$ , and molar concentration,  $C$ , which are all based on the KKS model [54]. In this work, since the free energy density is a function of concentration only, so will the Ginzburg-Landau free energy functional. If  $\beta$  is the gradient free energy, then it is defined as –

$$F = \int_V \left( f(C) + \frac{1}{2} \beta (\nabla C)^2 + \rho \phi \right) dV \quad (8)$$

Where  $f(C)$  is the free energy density. The equation for free energy density equation developed for this work is a function of molar concentration,  $C$ , only and defined as –

$$f(C) = W \left[ \left( \frac{C - C_1}{C_s - C_1} \right)^2 \left( \frac{C - C_s}{C_1 - C_s} \right)^2 \right] \quad (9)$$

Where  $C_1$  and  $C_s$  represent the concentration of  $\text{Li}^+$  in the electrolyte and electrode respectively in terms of mole fractions, and  $W$  represents the height of the double well potential function, shown in Figure 5.1. The height of the double well represents the amount of energy that is required for one phase to transform into another. The Gibbs free

energy is a function of electric potential,  $\phi$ , i.e. the driving force for the electrodeposition process, which is

$$\rho = zFC \quad (10)$$

Where  $z$  is the charge number of the lithium ion,  $F$  is the Faraday's constant and  $C$  is the concentration of  $\text{Li}^+$  ions in the system.

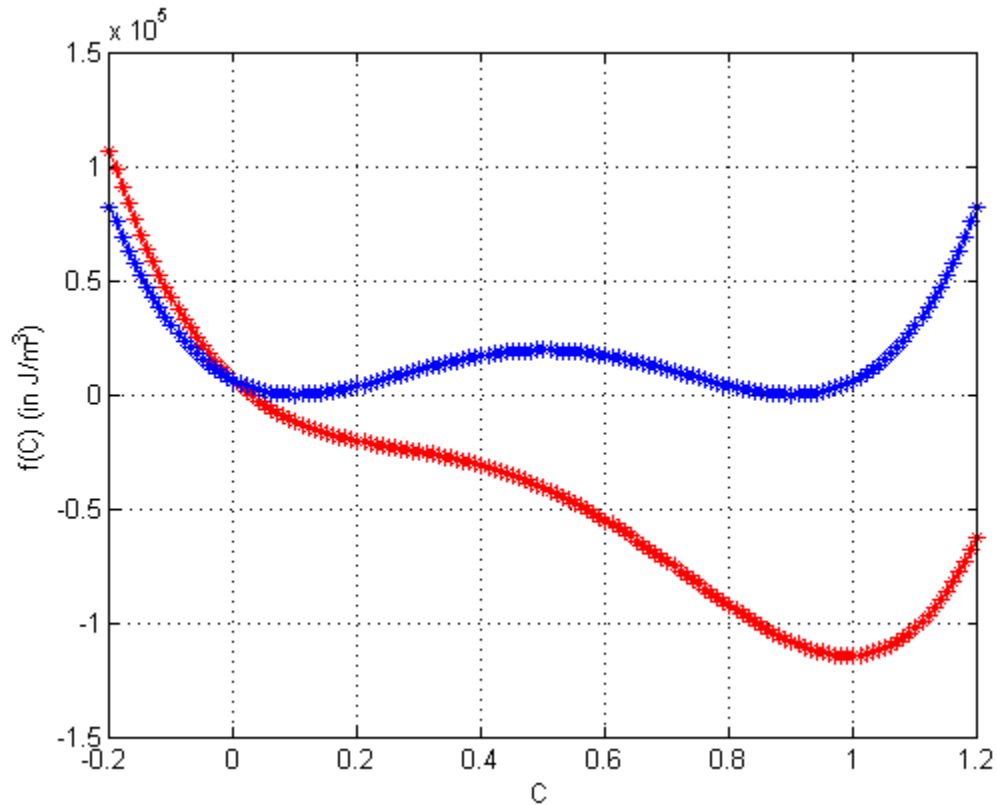


Figure 5.1. Free energy density without applied potential (blue curve) and with applied potential (red curve) of 0.1V vs. concentration

The liquid phase is assumed to be more dilute than the solid phase. The mole fractions of the components is employed here, given by:

$$\sum_{i=1}^n X_i = 1 \quad (11)$$

Where  $n$  represents the number of constituents in the system ( $n=2$ ). As the mole fractions varies from solid to liquid phase, so does the molar volume,  $V_m$ .

$$V_m = \sum_{i=1}^n \bar{V}_i X_i \quad (12)$$

$\bar{V}_i$  represents the partial molar volume of each phase. The molar concentrations for each phase is defined by  $C_i = X_i/V_m$ . Therefore,

$$\sum_{i=1}^n C_i \bar{V}_i = 1 \quad (13)$$

This is very similar to the summation of order parameter is equal to one at any point in the system, as presented in Section 4.1. Since the free energy density defined for this work is only a function of concentration, the summation of concentrations of all species at any point in the system will be equal to one.

It is common knowledge that all systems would ideally want to be stable. For a system to be thermodynamically stable, it is driven by minimization of its free energy. Figure 5.1 shows a double well potential function and the effect of a driving force. The function,  $f$ , plotted as the blue curve in Figure 5.1, indicates that the system has a minimum at both the electrolyte (liquid phase,  $C_l = 0.1$ ) and the electrode (solid phase,  $C_s = 0.9$ ), which means that both phases are stable when there is no applied voltage. For the  $\text{Li}^+$  ions in the liquid move towards the anode, they require sufficient energy to cross over the barrier, as shown, and settle into the more stable solid phase and form electrodeposits. The height of this barrier is the amount of energy required for transformation from liquid phase to solid phase. When a small voltage of 0.1V is applied to the system, the red curve in

Figure 5.1 shows that the minimum for the solid phase falls below that of liquid. This indicates that the solid phase is more stable than the liquid phase and has a lower free energy value when there is an applied voltage. This promotes the growth of solid phase i.e. electrodeposits in the system. The difference between free energies of the solid phase and liquid phase is the Gibbs free energy of the system.

## 5.2. GOVERNING EQUATIONS

The governing equation for concentration follows the fourth order Cahn-Hilliard equation since the concentration of  $\text{Li}^+$  ions is conserved in the system at any point of time. Using (4) and (9), the governing equation for concentration is derived and represented as

$$\frac{\partial C}{\partial t} = M \nabla^2 \left[ \frac{\partial f}{\partial C} - \beta (\nabla^2 C) \right] \quad (14)$$

Here M represents the diffusional mobility of  $\text{Li}^+$  ions and  $\Delta C = C_s - C_1$  is the difference between the concentrations in the electrode and electrolyte and is equal to 0.8 ( $C_s = 0.9$  and  $C_1 = 0.1$ ). A term,  $10000 \cdot \nabla C \cdot e^{-100(C+0.005)}$  is added inside (14) to ensure that the concentration does not drop below zero.

Since applied electric potential is the driving force for the electrodeposition process, an electroneutrality condition must be applied to indicate charge conservation in the system.

$$\nabla \cdot \mathbf{i} = 0 \quad (15)$$

given by the Laplace's equation, is defined to represent the distribution of electric potential in the entire domain, as given in [64].

$$\nabla \cdot [\varepsilon(C) \nabla \phi] = 0 \quad (16)$$



Where  $\varepsilon(C)$  is the electrical conductivity of the system as a function of molar concentration and  $\phi$  is the electric potential in the domain. The electrical conductivity of the system is a combination of electrical conductivities in electrode and electrolyte phases. It has been defined as:

$$\varepsilon(C) = \varepsilon_1 \frac{(C-C_1)^2}{(C_s-C_1)^2} + \varepsilon_s \frac{(C-C_s)^2}{(C_1-C_s)^2} \quad (17)$$

Where  $\varepsilon_1$  is the electrical conductivity in the electrolyte and  $\varepsilon_s$  is the electrical conductivity in the electrode. The discussion of their values will be made in the Section 5.3.

Equations (14) and (16) are the governing equations used in this work. For ease of computation, the non-dimensionalized forms of these equations are used and the non-dimensionalization procedure is established in Appendix A.

**5.2.1. Anisotropy in Cahn-Hilliard Equation.** For sufficiently strong anisotropic systems using the Cahn-Hilliard equation, a method of solving for anisotropy has been presented in [75, 76]. This method is a modification of the Kobayashi model method. It can not only predict microstructure growth for a four-fold (BCC) symmetry, but it can also predict six-fold (HCP) and eight-fold symmetries as well. If the gradient of  $C$  can be represented as  $\mathbf{p} = \nabla C$ , then the normal to this vector is given by  $\mathbf{n} = \frac{\mathbf{p}}{|\mathbf{p}|}$ , provided that

$|\mathbf{p}| \neq 0$ . The tangential projection matrix is given by

$$\mathbf{P} = \mathbf{I} - \mathbf{n} \otimes \mathbf{n} \quad (18)$$

For four-fold symmetry, the surface energy is given by

$$\gamma(\theta) = 1 + \delta \left( 4 \sum_{i=1}^d n_i^4 - 3 \right) \quad (19)$$

Where  $\delta$  is the strength of anisotropy and  $d=2, 3$  indicates the dimensional space defined.

In 2D, (19) is equivalent to

$$\gamma(\theta) = 1 + \delta \cos 4\theta \quad (20)$$

where  $\theta$  is the angle is made by the normal vector with the crystallographic axis. Since lithium has a BCC structure, the mode of anisotropy is equal to 4, meaning it has a four-fold symmetry. The value of  $\delta$  is chosen to be 0.3. since we consider a strongly anisotropic system. The crystallographic orientation is given by

$$\theta = \tan^{-1} \left( \frac{C_y}{C_x} \right) \quad (21)$$

Where  $C_x$  and  $C_y$  are the partial derivatives of concentration with respect to the x-axis and y-axis respectively. Therefore, the governing equation for concentration can be rewritten as

$$\frac{\partial C}{\partial t} = \nabla \cdot \mathbf{M} \nabla \cdot (f'(C) - \beta \nabla \cdot \mathbf{m}) \quad (22)$$

Where

$$\mathbf{m} = \gamma(\theta) \mathbf{p} - |\mathbf{p}| \mathbf{P} \nabla_{\theta} \gamma(\theta) \quad (23)$$

Substituting (23) in (22), we get

$$\frac{\partial C}{\partial t} = \nabla \cdot \left( \mathbf{M} \nabla \cdot (f'(C) - \beta \nabla \cdot [\gamma(\theta) \nabla C + \gamma'(\theta) |\nabla C| \mathbf{P}]) \right) \quad (24)$$

Equations (24) and (16) serve as the governing equations for the system now.

### 5.3. SIMULATION PARAMETERS AND BOUNDARY CONDITIONS

The boundary conditions employed in the simulation are zero-flux boundary conditions for the concentration equation. Since a small portion of the battery is being

simulated, periodic boundary conditions are applied to top and bottom side of the domain to denote that the same profile trends will be followed in the vertical direction. For the potential, a Dirichlet boundary condition is applied at the left and right boundaries and ensure they are maintained at a constant value throughout the simulation. The system is isothermal and set at room temperature of 298 K. The simulations have been run using COMSOL Multiphysics 5.0 and 5.1.

From the equations provided in [72], the surface energy ( $\gamma$ ) and thickness ( $2\lambda$ ) of the interface are calculated. These equations are similar to those put forth by Kim et al. for the solidification process.

$$\gamma = \sqrt{\frac{\beta W}{18}} \quad (25)$$

$$2\lambda = \sqrt{\frac{8\beta}{W}} \quad (26)$$

Substituting the appropriate values given in Table 5.1 in the above two equations, the surface energy is  $0.001 \text{ J/m}^2$  and the thickness of the interface between the two phases is  $0.569 \text{ }\mu\text{m}$ . Table 5.2 mentions the constants used in the simulations.

Table 5.1 Values of Parameters used in the Simulations

Parameter	Representation	Value
Gradient energy coefficient	$\beta$	$1 \times 10^{-9} \text{ J/m}$
Height of the double well	$W$	$2.475 \times 10^4 \text{ J/m}^3$
Electrical conductivity in electrode	$\epsilon_s$	$1.1 \times 10^7 \text{ S/m}$

Table 5.1. Values of Parameters used in the Simulations (contd.)

Electrical conductivity in electrolyte	$\epsilon_1$	1.07 S/m
---	--------------	----------

Table 5.2 Values of Constants used in the Simulations

Parameter	Representation	Value
Gas constant	R	8.314 J/mol.K
Temperature	T	298 K
Faraday's constant	F	96500 C/mol
Charge number of lithium	z	1
Diffusion coefficient of Li <sup>+</sup> in the electrolyte	D	1x10 <sup>-10</sup> m <sup>2</sup> /s

## 6. RESULTS AND DISCUSSIONS

### 6.1. CONVERGENCE STUDY

In computational modeling involving partial differential equations (PDEs), discretizing the domain is the important step in obtaining an accurate solution. Discretization divides the domain into small elements and the PDEs are computed at every element in the domain and provides us a solution of the PDEs at each and every element in the domain.

The shapes of mesh to be used depends on the types of equations being solved i.e. a two-dimensional or a three-dimensional equation. The common element shapes for a 2D problem are triangle and quadrilateral. The common element shapes for a 3D problem are tetrahedron, pyramid, triangular prism and hexahedron. They are shown in Figure 6.1 and Figure 6.2 respectively.

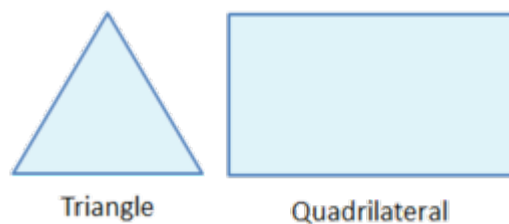


Figure 6.1. Element shapes used in 2D analysis

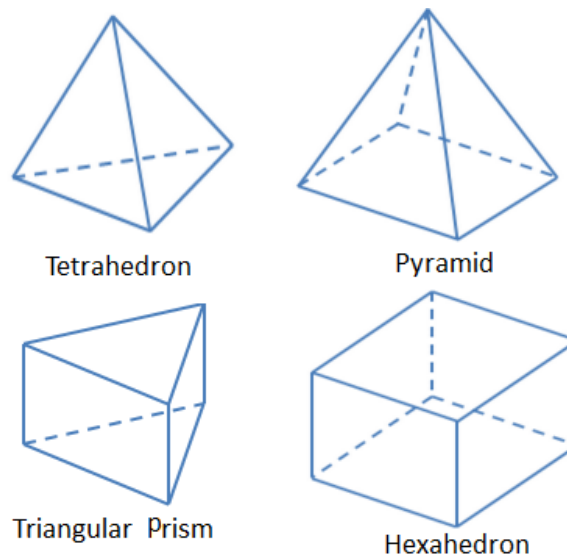


Figure 6.2. Element shapes used in 3D analysis.

The factors to be considered for selection of an optimum mesh size are:

- High convergence rate – The mesh size chosen should help in faster convergence of solution. There is a linear dependence on using a mesh of better quality and obtaining faster convergence solution.
- High accuracy of solution – Using a mesh with a smaller grid size will give a higher accuracy of solution than compared to a mesh with larger grid size. In a mesh, the partial differential equations are solved at each and every element in the domain. Higher the number of elements, greater will be the accuracy.
- Low computation time – Selecting a very fine mesh is not always desirable because it makes the computation time very long, which then requires a large amount of memory to run and store the solution on the computer. There is a trade-off involved in selecting a very fine mesh and computation time.

With knowledge of these factors, a mesh convergence study is performed to identify the optimum mesh size which would produce the most accurate solution without taking too much computational time and computer memory.

For the mesh convergence study, a 2D rectangular domain of  $158.9\mu\text{m} \times 6.356\mu\text{m}$  ( $50 \times 2$  in non-dimensionalized scale) is used to represent the lithium anode and electrolyte. A small layer is used to represent the anode and the rest of the domain represents the electrolyte. The mesh created is a mapped mesh with quadrilateral elements since there are no irregular boundaries present in the domain. Some of the advantages of using a mapped mesh are that it divides the whole domain into equal number of elements and has a regular pattern.

The use of a domain with a larger width will produce the same results as the one with  $50 \times 2$  since periodic boundary conditions have been applied at the top and bottom edges of the domain. Periodicity along the top and bottom edges ensures same thickness of growth of electrodeposited Li along the vertical direction. The main advantage of using a smaller width domain is decrease in computational time.

Modeling was started using a coarse mapped mesh of size 0.25 and worked down to a fine mapped mesh of size 0.04. It can be seen that the elements in the domain with mesh size 0.25 can be distinguished whereas the elements in the domain of mesh size 0.04 are so close to each other that individual elements cannot be discerned. The properties of the different mesh sizes are given in Table 6.1. Properties of different mesh sizes Note that mesh sizes are given in the non-dimensionalized scale.

Table 6.1. Properties of different mesh sizes.

Mesh size	Domain Elements	Boundary Elements	Degrees of Freedom
0.25	1,600	424	27,268
0.125	6,400	848	105,732
0.1	10,000	1,060	164,164
0.07	20,735	1,517	337,716
0.0625	25,600	1,696	416,260
0.05	40,000	2,120	648,324
0.04	62,500	2,650	1,010,404

Simulations are performed for each case for time of 3.03s (30s in non-dimensionalized scale). The thicknesses of the layer formed due to deposition of  $\text{Li}^+$  ions are plotted after 2.02s (20s in non-dimensionalized scale) against the inverse of the mesh density and is shown in Figure 6.3. While performing these simulations, it is important to know that anisotropy was not applied to the system and hence, there was no microstructure growth but just the growth of a homogeneous layer from the surface of the lithium metal anode. Each case was run with a constant potential of 0.2V applied at the right boundary of the system, a constant electrolyte mole fraction of 0.1 and zero flux boundary conditions for concentration. The governing equations used for the convergence study are (14) and (16).



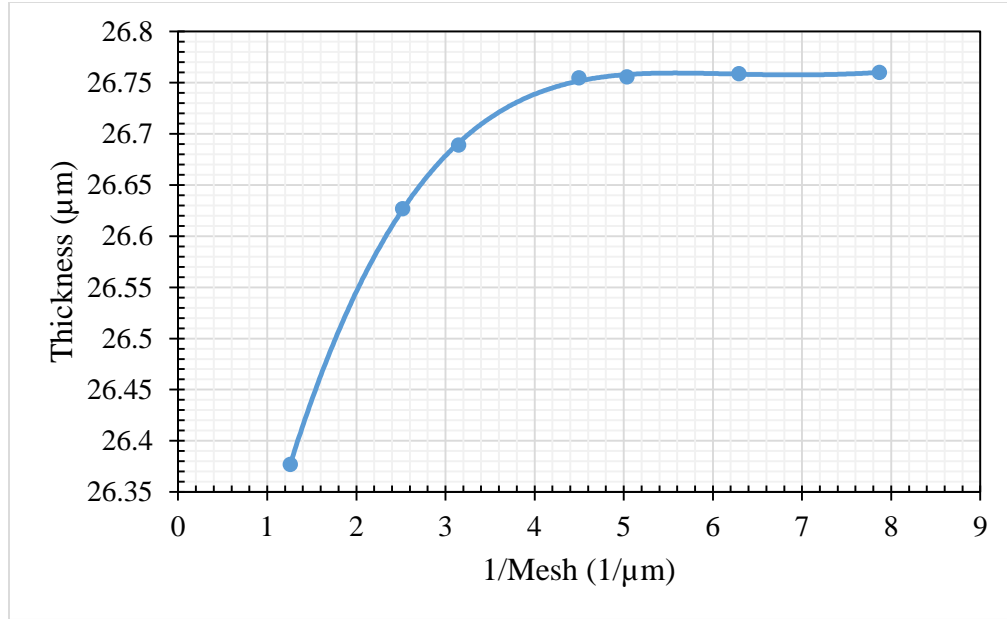


Figure 6.3. Thickness vs. (1/Mesh).

From the above graph, it can be concluded that convergence occurs when the inverse of mesh density is 4.49 (1/μm). Therefore, the optimum mesh size is  $(1/4.49519) = 0.22 \mu\text{m}$ , which is 0.07 in non-dimensionalized scale.

## 6.2. EFFECT OF DIFFERENT ELECTRICAL CONDUCTIVITY RATIOS

From the results of the mesh convergence study, the mesh size of 0.07 has been employed for all further simulations in this work. Firstly, the effect of growth from the anode surface by using different electrical conductivity ratios is measured. It is common knowledge that the electrical conductivity of pure lithium is  $1.1 \times 10^7 \text{ S/m}$ , which is that of the electrode. The electrolyte is a mixture of lithium hexafluorophosphate (LiPF<sub>6</sub>) in a binary organic electrolyte.

As discussed in Chapter 2, organic electrolytes have very low electrical conductivities and hence, the conductivity of the electrolyte is the conductivity of the Li salt present. In this study, the electrical conductivity of the electrolyte in the Li metal battery is 1.07 S/m, which is the electrical conductivity of lithium hexafluorophosphate (LiPF<sub>6</sub>) and this has been discussed in Chapter 2. Hence, the ratio of electrical conductivity of electrode to that of the electrolyte is  $1 \times 10^7$ .

$$\text{Electrical Conductivity Ratio} = \frac{\epsilon_s}{\epsilon_1} \quad (27)$$

Where  $\epsilon_s$  is the electrical conductivity of the electrode and  $\epsilon_1$  is the electrical conductivity of the electrolyte. Since the computation using the value of  $1e7$  in the simulations becomes too cumbersome, the effects of 6 electrical conductivity ratios –  $1 \times 10^2$ ,  $1 \times 10^3$ ,  $1 \times 10^4$ ,  $1 \times 10^5$ ,  $1 \times 10^6$  and  $1 \times 10^7$  – have been studied and the thicknesses obtained using each ratio has been recorded and plotted in a graph below as a function of time. The thickness for each case is measured after 2.02s and recorded and plotted in Figure 6.4. The simulations were performed for zero flux of concentration and applied voltage of 0.2V.

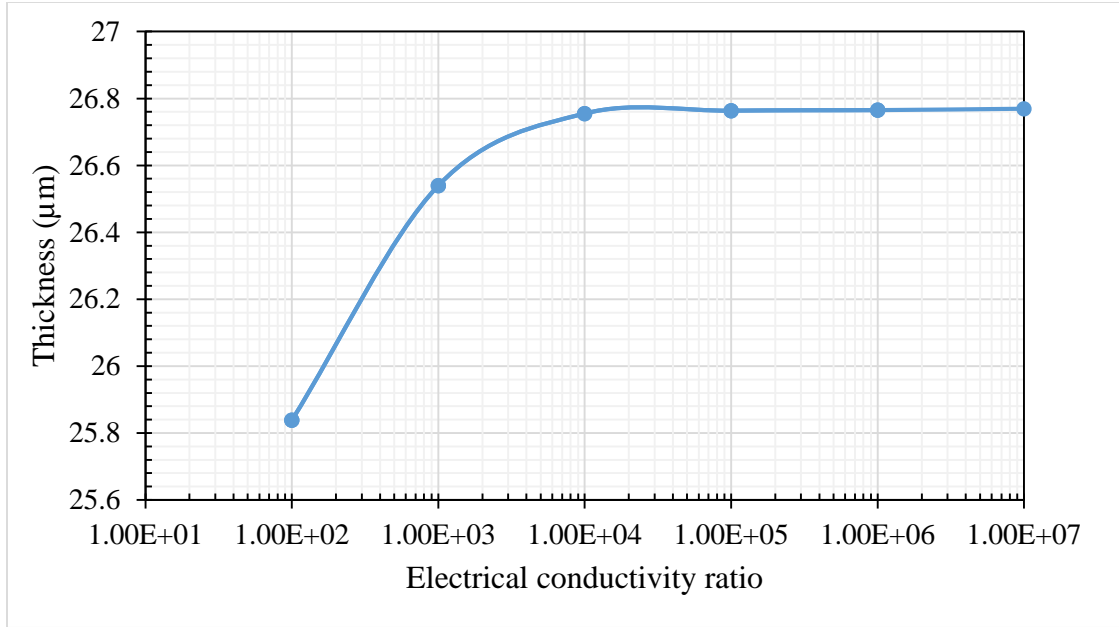


Figure 6.4. Thickness vs different electrical conductivity ratios.

The thickness is plotted as a function of electrical conductivity ratio on a logarithmic scale. From Figure 6.4, it can be seen that from a conductivity ratio of  $1e4$ , all higher conductivity ratios produced same or similar thicknesses. Hence, all subsequent simulations are carried out using a conductivity ratio of  $1e4$ .

### 6.3. EFFECT OF DIFFERENT BOUNDARY CONDITIONS FOR CONCENTRATION FIELD

Although the simulations were carried out using a zero flux boundary condition for concentration for the mesh convergence and testing of effects of different ratios of electrical conductivity, we now want to test the effects of changing the boundary condition for concentration on the right edge of the domain, on the growth thickness. The effects of three different boundary conditions are studied – zero flux boundary condition, Dirichlet

boundary condition and a constant flux (Neumann) boundary condition. These conditions are simulated for three values of constant applied voltage – 0.1V, 0.2V and 0.3V. An applied voltage at the cathode not only dissociates lithium cations, but also creates an electric field which pushes these dissociated cations in a particular direction, in this case towards the anode. The Li salt in the electrolyte is also broken up into anions and cations on application of a voltage. Three increasing voltages are applied to study the effects of an increasing electric field on the electrodeposition process. The source term of potential is zero, as mentioned in the governing equation. Comparisons are made by plotting growth thickness vs. time and growth rate vs. applied potential for different cases.

### **6.3.1. Zero Flux Boundary Condition for Concentration and Applied**

**Voltages of 0.1V, 0.2V and 0.3V.** Figure 6.5 shows that the growth thickness is directly proportional to applied voltage.

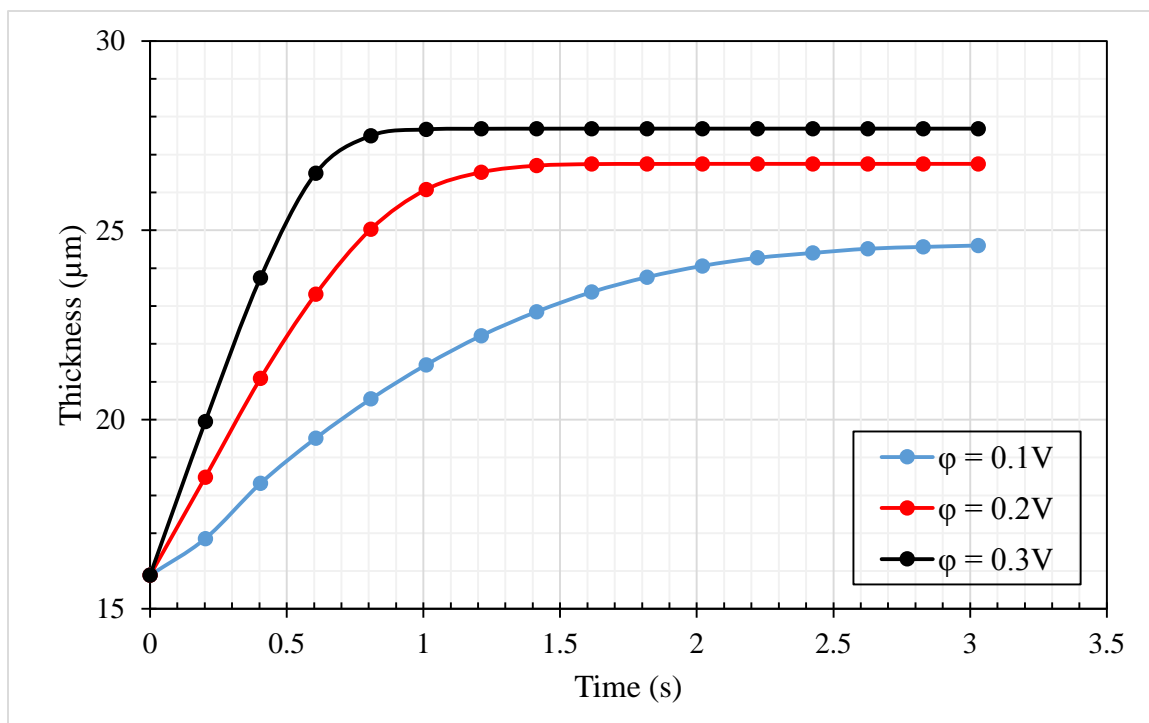


Figure 6.5. Growth thickness vs. time for different applied voltages and zero flux of concentration

However, the growth trend for 0.1V is different from that of 0.2V and 0.3V. For the duration of 3.03s, the applied voltage of 0.1V is a small driving force i.e. creates a small electric field for  $\text{Li}^+$  ions to dissociate in the electrolyte and flow towards the electrode. Hence, fewer  $\text{Li}^+$  ions dissociate and get slowly deposited and this is shown by the curve which linearly increases at first and slowly starts becoming parabolic. It is seen that at 3.03s, the thickness for an applied potential is 23.36  $\mu\text{m}$  and some cations are still depositing on the electrode surface.

For an applied voltage of 0.2V, more number of  $\text{Li}^+$  ions dissociate but the driving force is quite large that all the dissociated  $\text{Li}^+$  ions deposit on the electrode faster until there are no  $\text{Li}^+$  ions left in the system. Hence, this curve increases linearly and approaches a

constant value at 2.02s i.e. all free  $\text{Li}^+$  ions get deposited on the electrode surface after 2.02s itself, unlike the case for 0.1V.

For an applied potential of 0.3V, even more number of  $\text{Li}^+$  ions dissociate from the cathode surface and the driving force and hence, electric field, is so large that all the dissociated  $\text{Li}^+$  ions deposit on the electrode faster until there are no free  $\text{Li}^+$  ions left in the system. Hence, this curve increases linearly, has a higher slope and approaches a constant value at 1.616s, faster than the case with applied voltage of 0.2V. The differences between thicknesses after 1.616s for 0.1V, 0.2V and 0.3V applied voltages are 23.36  $\mu\text{m}$ , 26.74  $\mu\text{m}$  and 27.68  $\mu\text{m}$ .

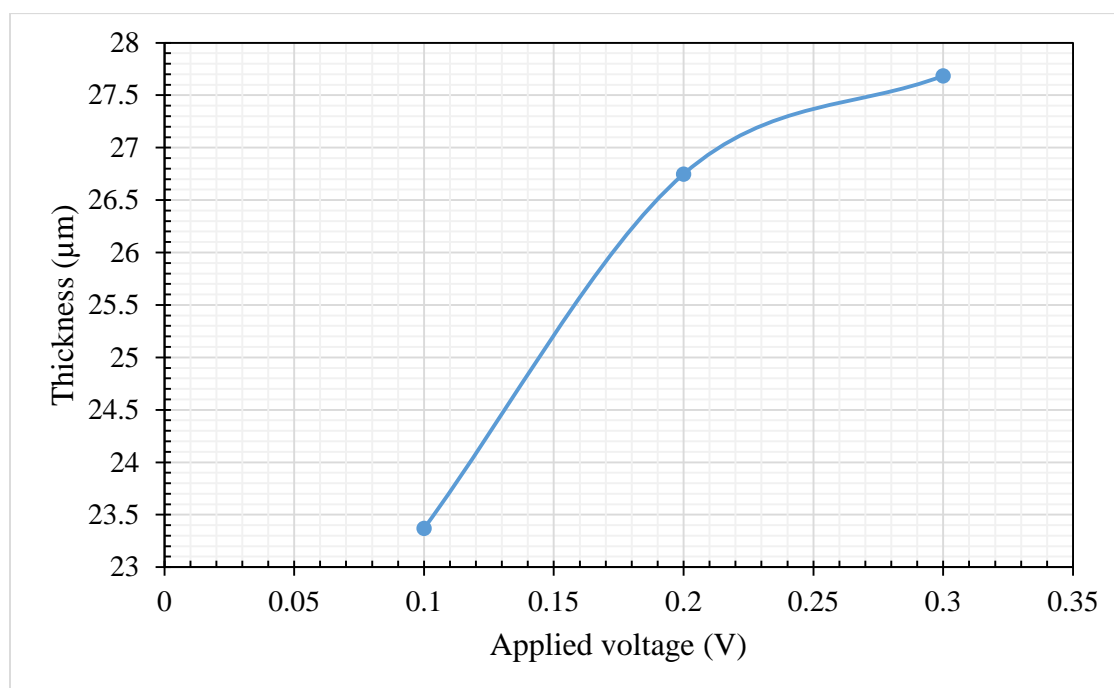


Figure 6.6. Thickness vs. applied voltage for zero flux of concentration

Figure 6.7 shows how the growth thickness varies as a function of applied voltage after 1.616s. The difference in growth thickness is much larger between 0.1V and 0.2V when compared to that between 0.2V and 0.3V. As explained previously, as the driving force increases, so does the thickness. But a limiting value is reached as the applied voltages are increased because the system only has finite number of  $\text{Li}^+$  ions. To get a better idea of the variation in thicknesses, the values of growth rate for different applied potentials after 1.616s are plotted in Figure 6.7. Growth rate vs. applied voltage for zero flux of concentration.

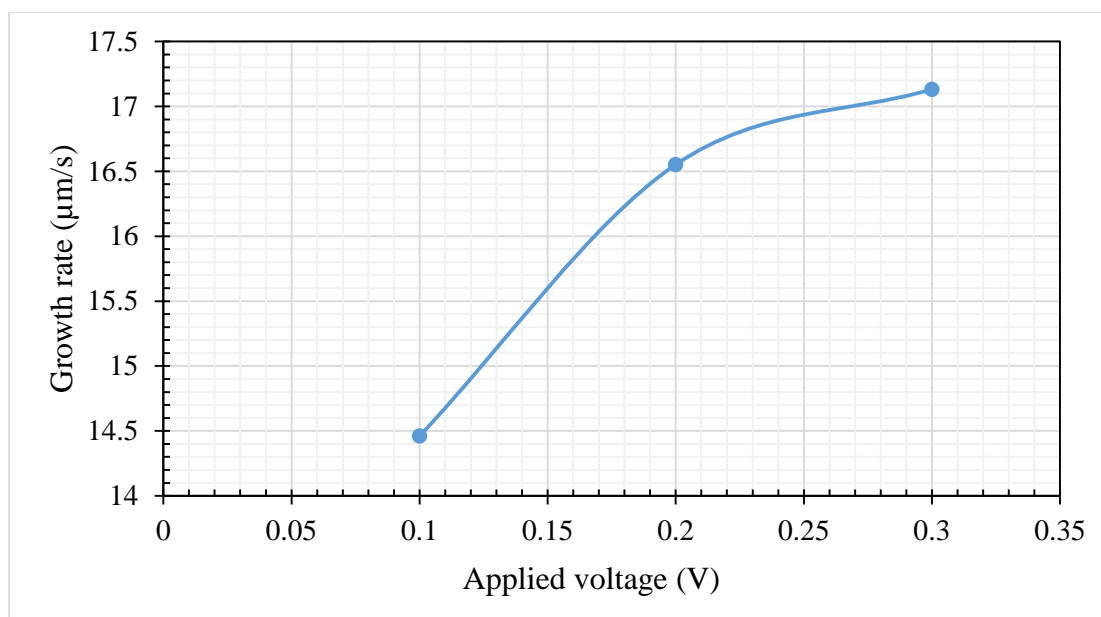


Figure 6.7. Growth rate vs. applied voltage for zero flux of concentration

There is a very high increase in growth rate from 0.1V to 0.2V, as seen in Figure 6.7, and as the case with thickness, the difference in growth rate between two consecutive values of applied voltage deteriorates as the applied potentials increase.

All the profiles for potential can be divided into three regimes – (a) Due to the high conductivity of the electrode, a uniform potential distribution is observed in the electrode, (b) The low conductivity of the electrolyte results in a gradient change in the distribution of electric potential and (c) At the interface, a step is observed, which signifies a potential drop due to the reaction that occurs at the interface caused by the  $\text{Li}^+$  ions that accumulate at the interface over time. All the profiles for electric potential follow this trend i.e. Figure 6.10, Figure 6.13 and Figure 6.16 show the potential profiles for applied voltages of 0.1V, 0.2V and 0.3V respectively.

The thicknesses in the domains have also been illustrated to observe how the electrodeposits grow as time passes. They have been plotted to show the variation of growth thicknesses in the concentration and potential domains. Figure 6.8, Figure 6.11 and Figure 6.14 show the variation of growth thicknesses in the concentration field for applied voltages of 0.1V, 0.2V and 0.3V respectively. Figure 6.9, Figure 6.12 and Figure 6.15 show the variation of growth thicknesses in the potential field for applied voltages of 0.1V, 0.2V and 0.3V respectively.





Figure 6.8. Concentration profiles at  $t=0$  (top),  $t=0.808\text{s}$  (middle) and  $t=1.616\text{s}$  (bottom) for zero flux boundary condition for  $\phi=0.1\text{V}$

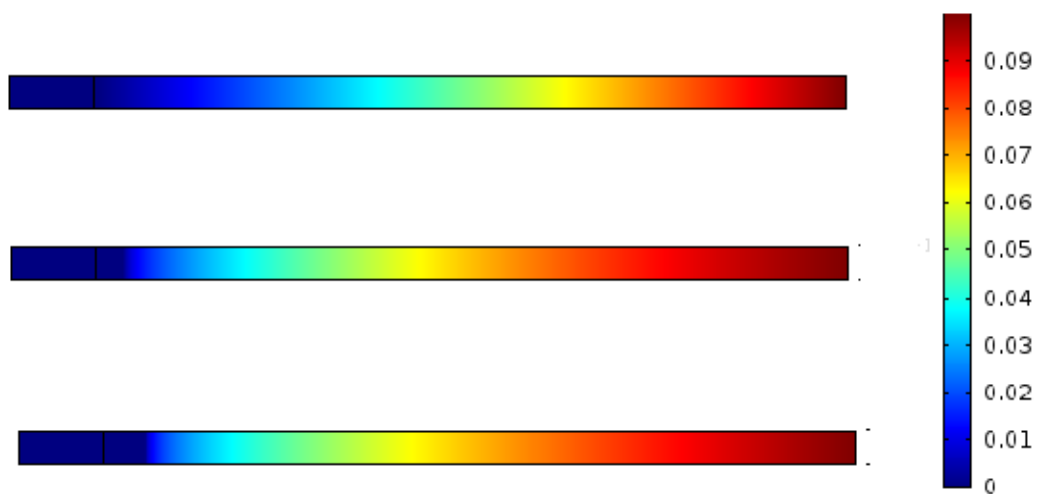


Figure 6.9. Potential profiles at  $t=0$  (top),  $t=0.808\text{s}$  (middle) and  $t=1.616\text{s}$  (bottom) for zero flux boundary condition for  $\phi=0.1\text{V}$

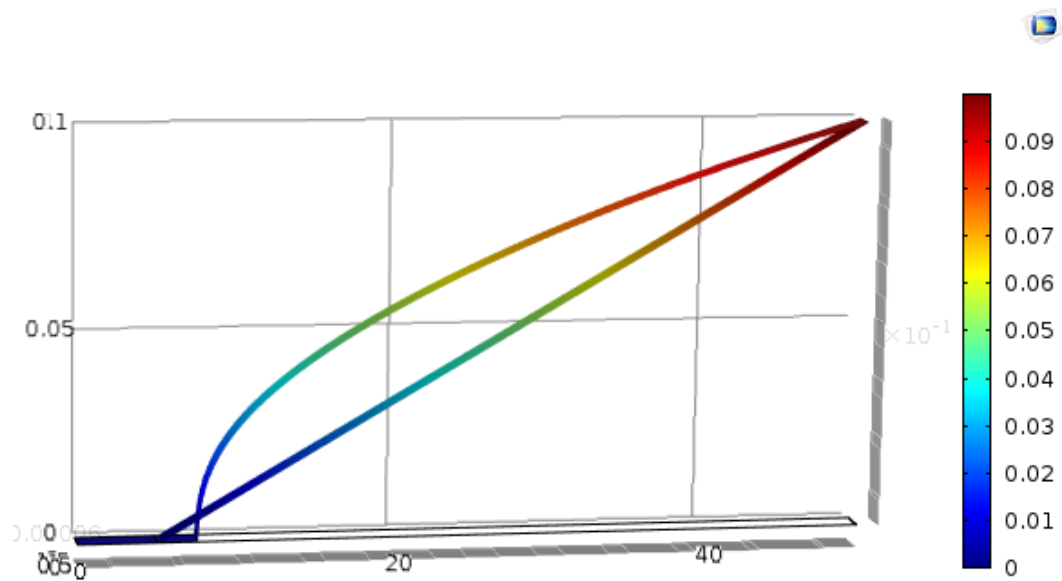


Figure 6.10. Potential profiles at  $t=0$  and  $t=1.616\text{s}$  for zero flux boundary condition for  $\phi=0.1\text{V}$

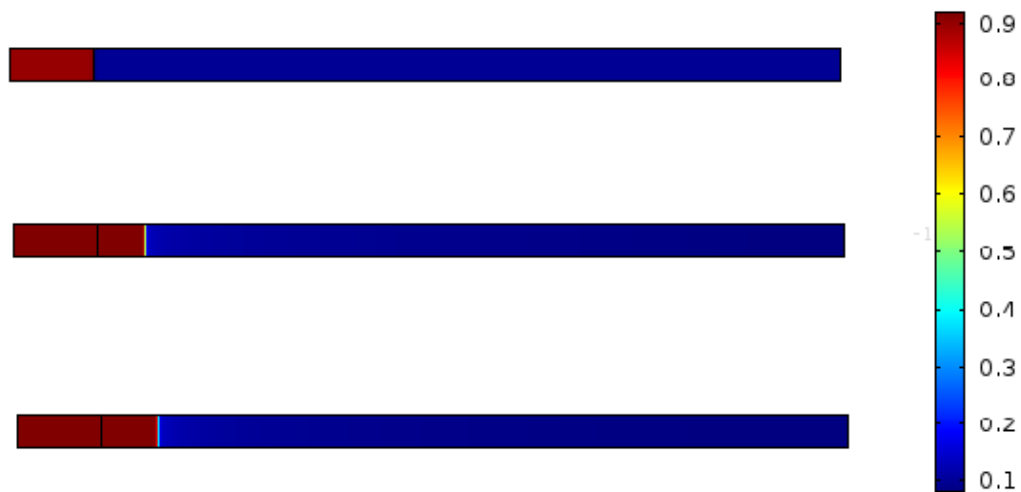


Figure 6.11. Concentration profiles at  $t=0$  (top),  $t=0.808\text{s}$  (middle) and  $t=1.616\text{s}$  (bottom) for zero flux boundary condition for  $\phi=0.2\text{V}$

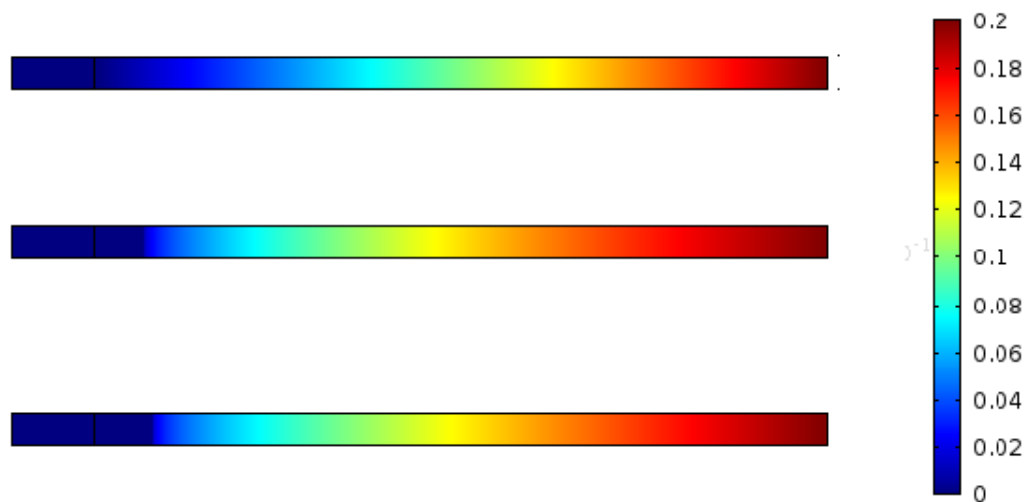


Figure 6.12. Potential profiles at  $t=0$  (top),  $t=0.808\text{s}$  (middle) and  $t=1.616\text{s}$  (bottom) for zero flux boundary condition for  $\phi=0.2\text{V}$

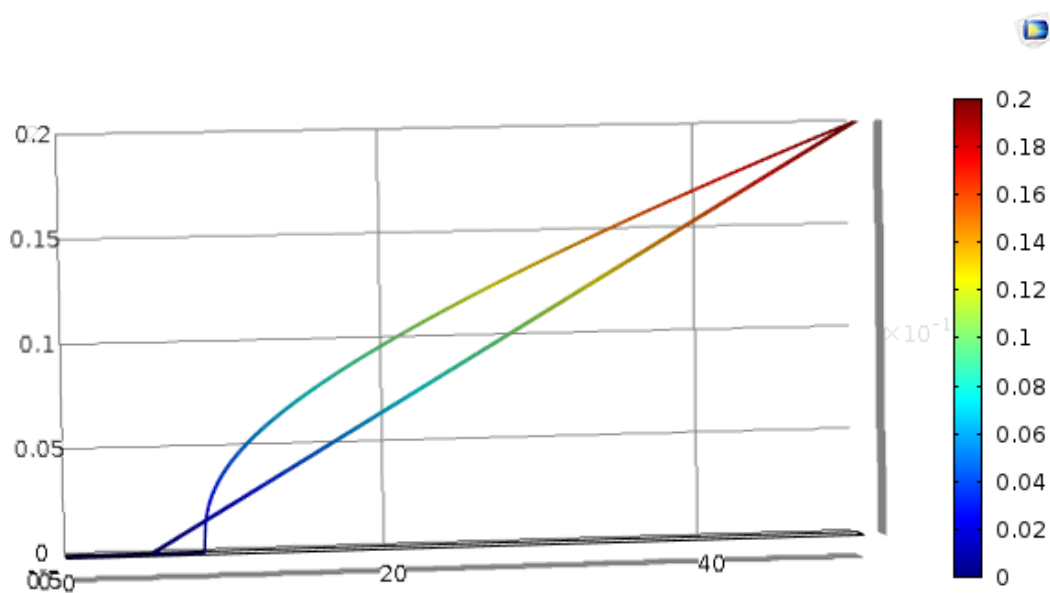


Figure 6.13. Potential profiles at  $t=0$  and  $t=1.616\text{s}$  for zero flux boundary condition for  $\phi=0.2\text{V}$

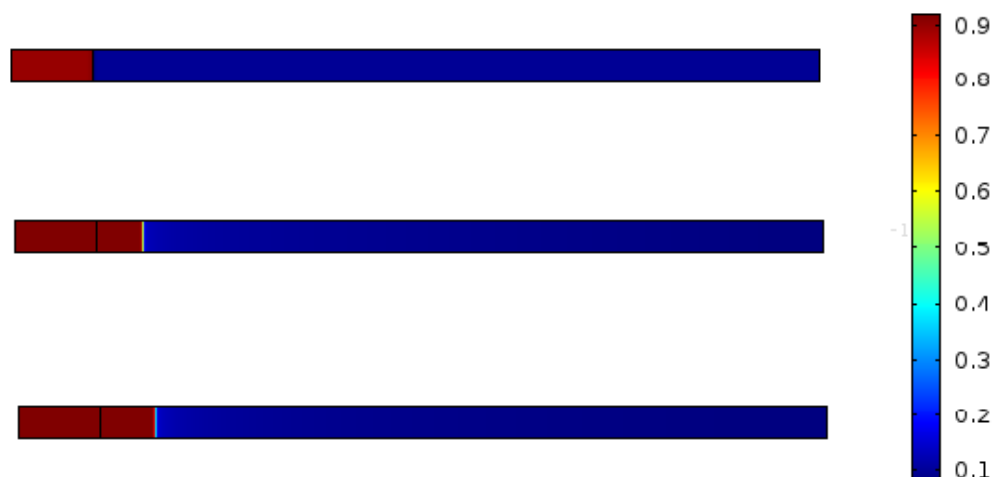


Figure 6.14. Concentration profiles at  $t=0$  (top),  $t=0.808\text{s}$  (middle) and  $t=1.616\text{s}$  (bottom) for zero flux boundary condition for  $\phi=0.3\text{V}$

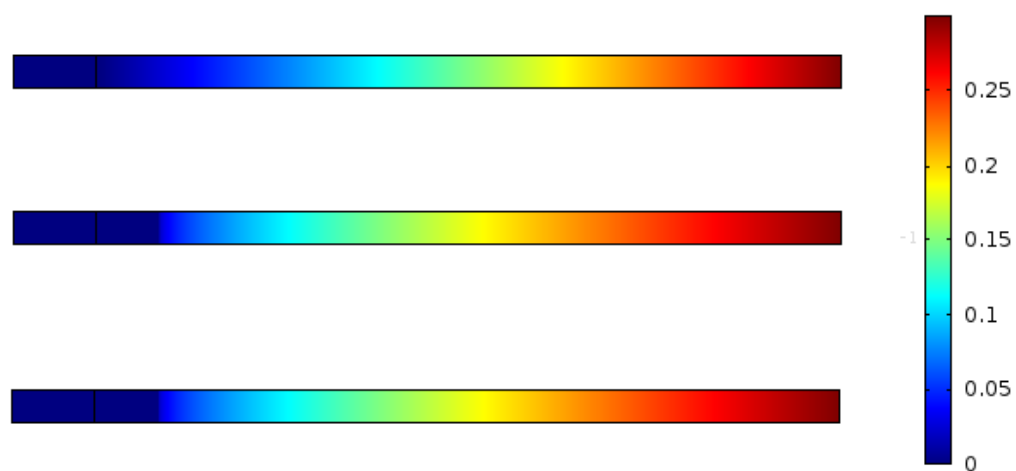


Figure 6.15. Potential profiles at  $t=0$  (top),  $t=0.808\text{s}$  (middle) and  $t=1.616\text{s}$  (bottom) for zero flux boundary condition for  $\phi=0.3\text{V}$

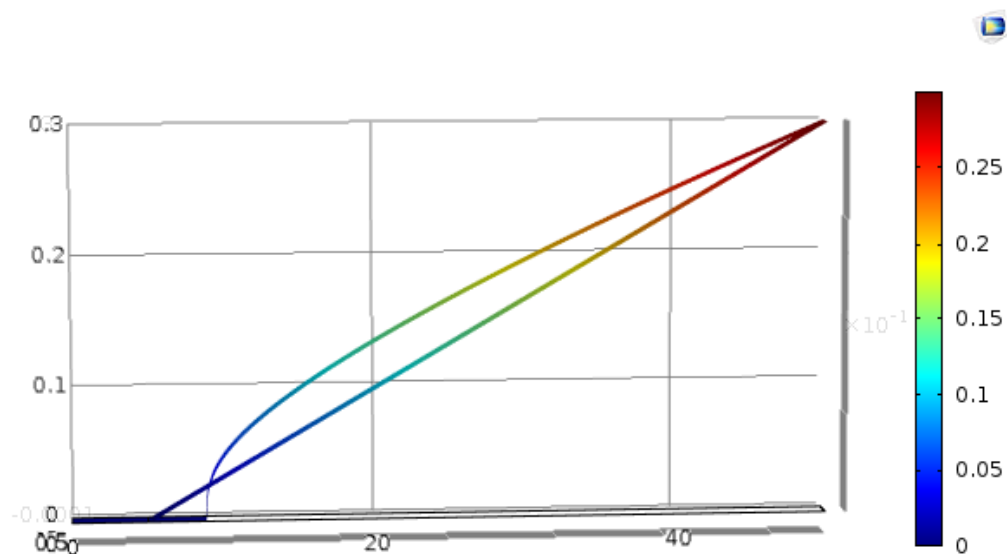


Figure 6.16. Potential profiles at  $t=0$  and  $t=1.616$ s for zero flux boundary condition for  $\phi=0.3$ V

**6.3.2. Dirichlet Boundary Condition for Concentration and Applied Voltages of 0.1V, 0.2V and 0.3V.** The application of a Dirichlet boundary condition at the right boundary for concentration implies that the concentration is maintained fixed a constant number of  $\text{Li}^+$  ions will always flow from the cathode towards the anode at the specified value without decrease over time. In this case, the Dirichlet boundary condition was maintained at the same value as the concentration of the electrolyte i.e. 0.1 and it is plotted in Figure 6.17.

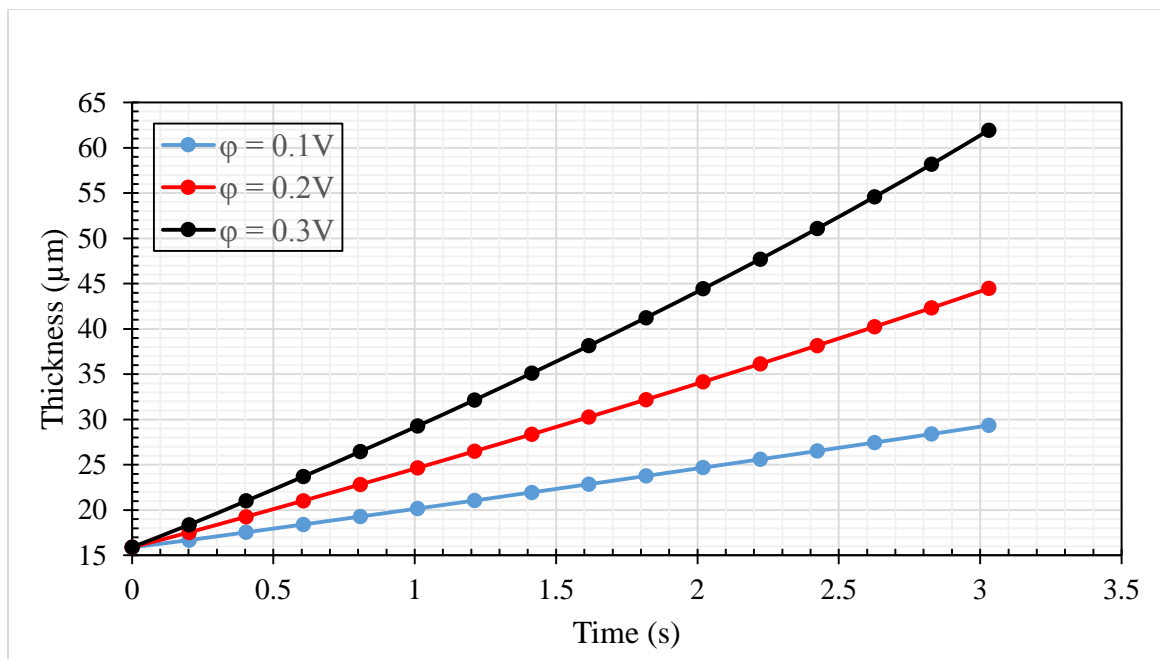


Figure 6.17. Growth thickness vs time for different applied potentials for Dirichlet boundary condition of concentration.

Figure 6.17 clearly defines a Dirichlet boundary condition. It can be seen that the growth thickness is directly proportional to time and the curves are always increasing linearly since there is constant flow of  $\text{Li}^+$  ions from the cathode to the anode. However, this is not a practical scenario as the electrolyte is not infinitely stocked with lithium, but will get depleted of all its lithium over time. There is also no distinction between differences in thicknesses between the 3 voltages, as seen in the case with zero flux boundary condition. Figure 6.18 shows the values and trend of growth thicknesses for different values of applied potentials after 3.03s.

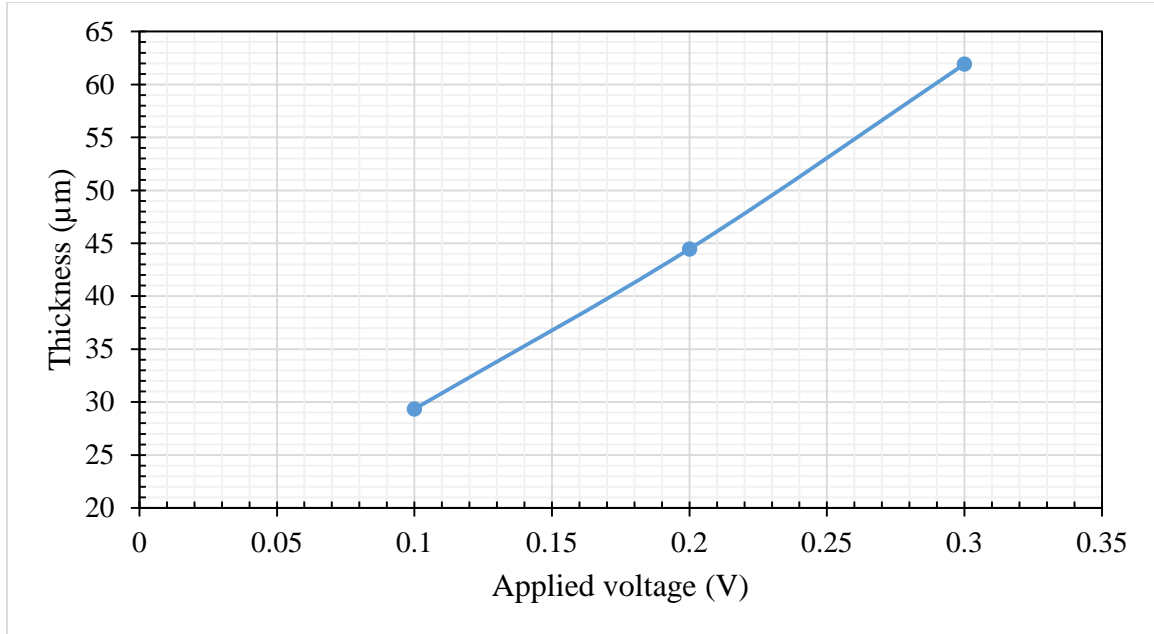


Figure 6.18. Growth thickness vs applied voltage for Dirichlet boundary of concentration

Since the growth thickness varies linearly with respect to time, so will the growth rate, whose values are plotted in Figure 6.19.

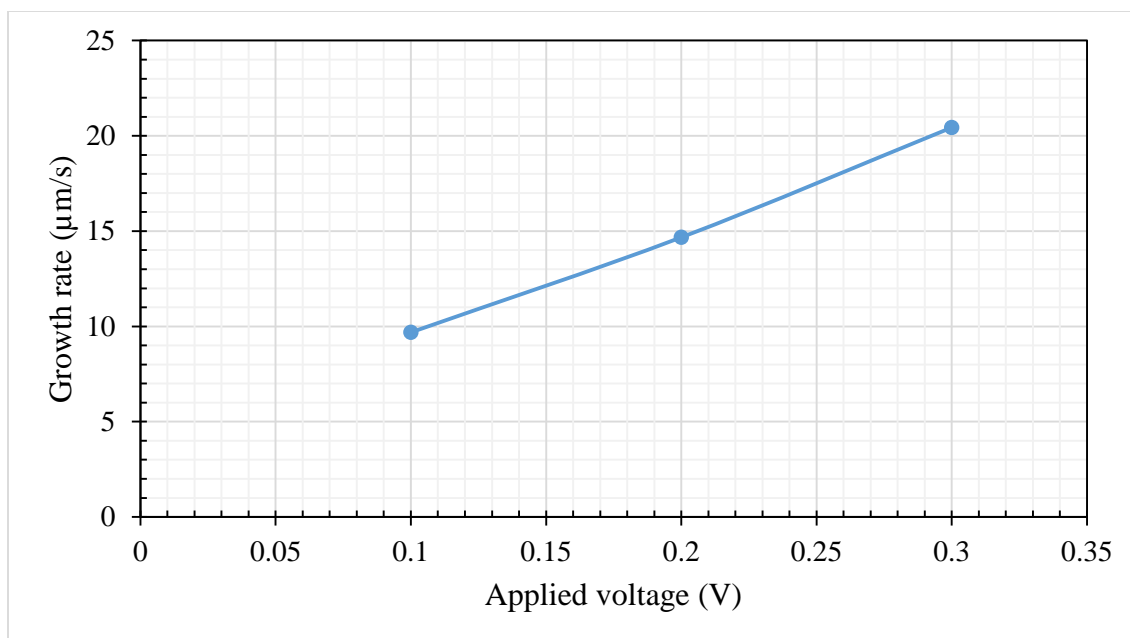


Figure 6.19. Growth rate vs applied potentials for Dirichlet boundary of concentration



**6.3.3. Constant Flux (Neumann) Boundary Condition for Concentration and Applied Voltages of 0.1V, 0.2V and 0.3V.** Flux is rate of flow of a certain quantity per unit time. In this case, a flux of concentration is considered and a magnitude of concentration is applied as a boundary condition instead of a zero flux or Dirichlet boundary condition. To test the effect on thickness by adding a flux to the right boundary of concentration, three different flux magnitudes of 0.01 mol/m<sup>2</sup>s (low), 0.05 mol/m<sup>2</sup>s (medium) and 0.1 mol/m<sup>2</sup>s (high) are applied to gain a more accurate idea of the effects of a concentration flux. The simulations are performed for the aforementioned values of concentration flux and for the three different applied voltages – 0.1V, 0.2V and 0.3V. This is mainly done to see the effect of different fluxes on potential and vice-versa. The thicknesses are recorded after 3.03s. The concentration and potential profiles obtained from COMSOL Multiphysics are not included here since their trend matches the trend of the profiles provided for the zero flux boundary condition case. However, the plots of thickness vs. time for different applied voltages and fluxes are given from Figure 6.20 to Figure 6.25.

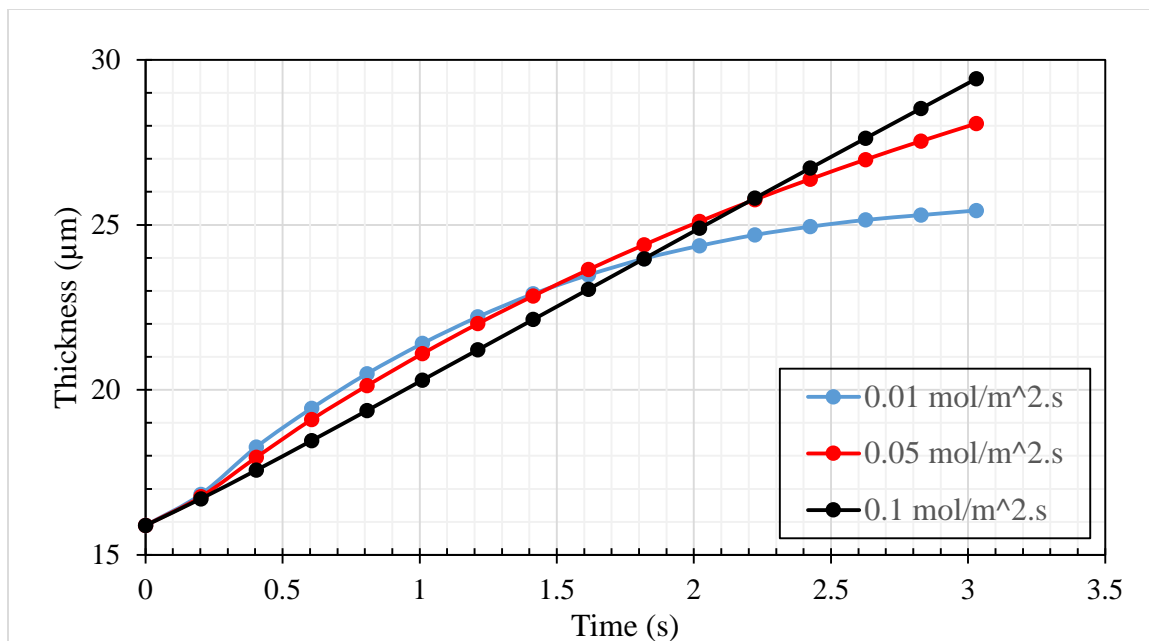


Figure 6.20. Thickness vs time for different fluxes at 0.1V

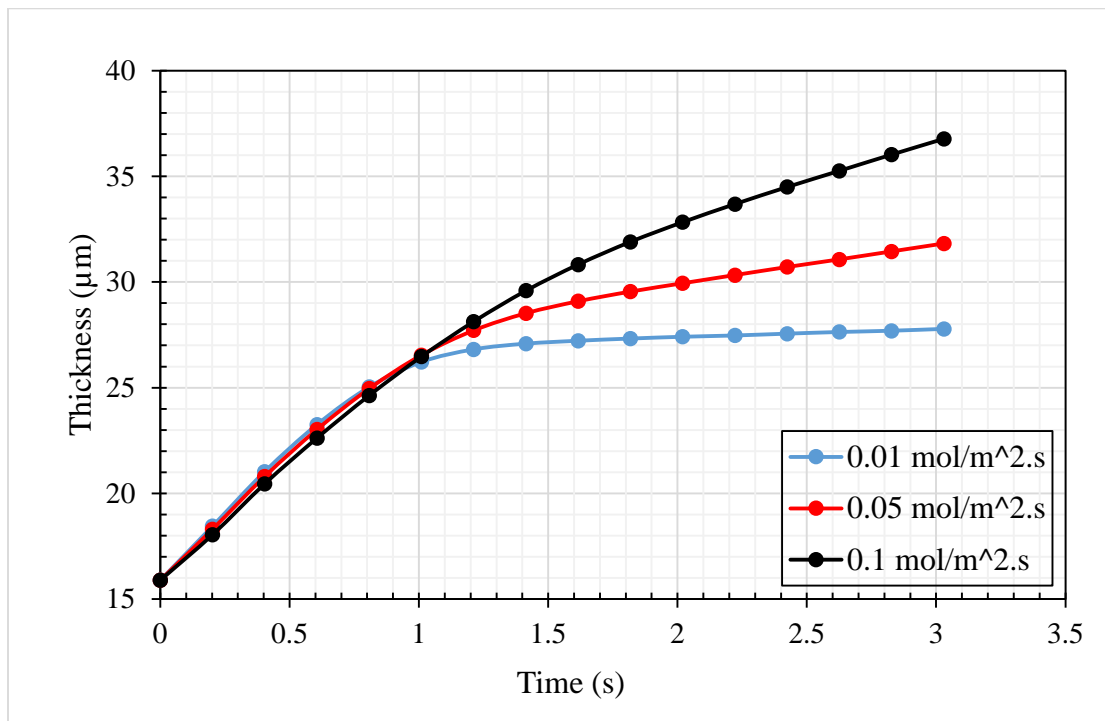


Figure 6.21. Thickness vs time for different fluxes at 0.2V

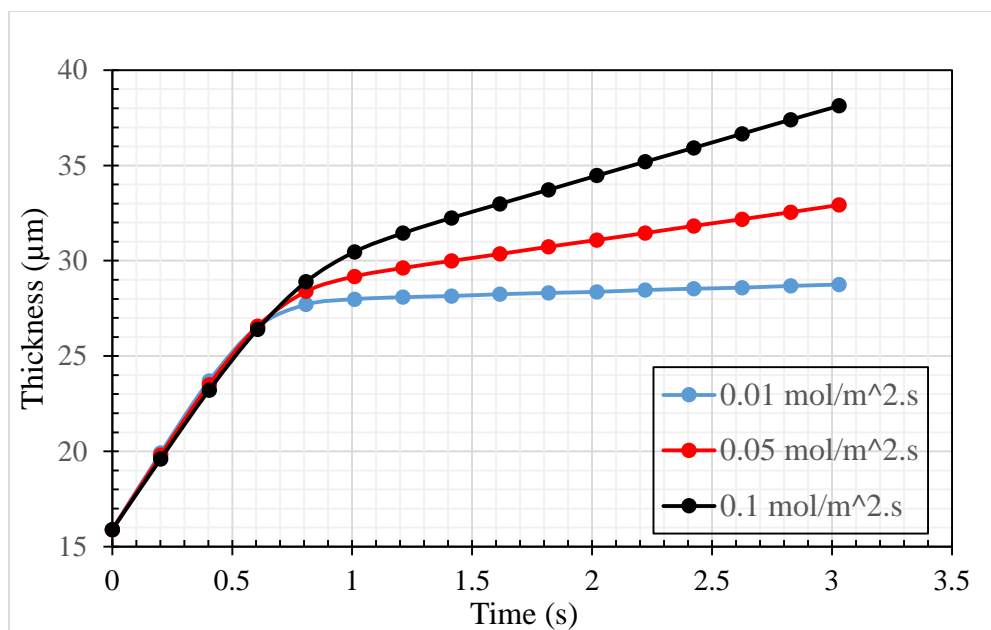


Figure 6.22. Thickness vs time for different fluxes at 0.3V

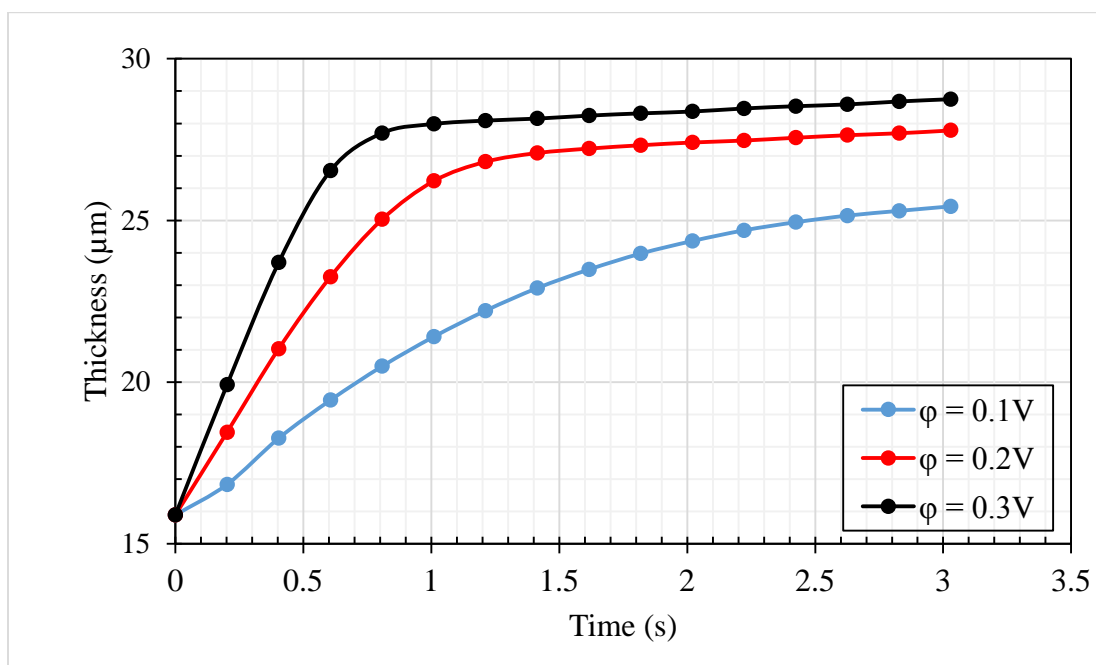


Figure 6.23. Thickness vs time for different voltages at  $0.01 \text{ mol/m}^2\cdot\text{s}$  flux.

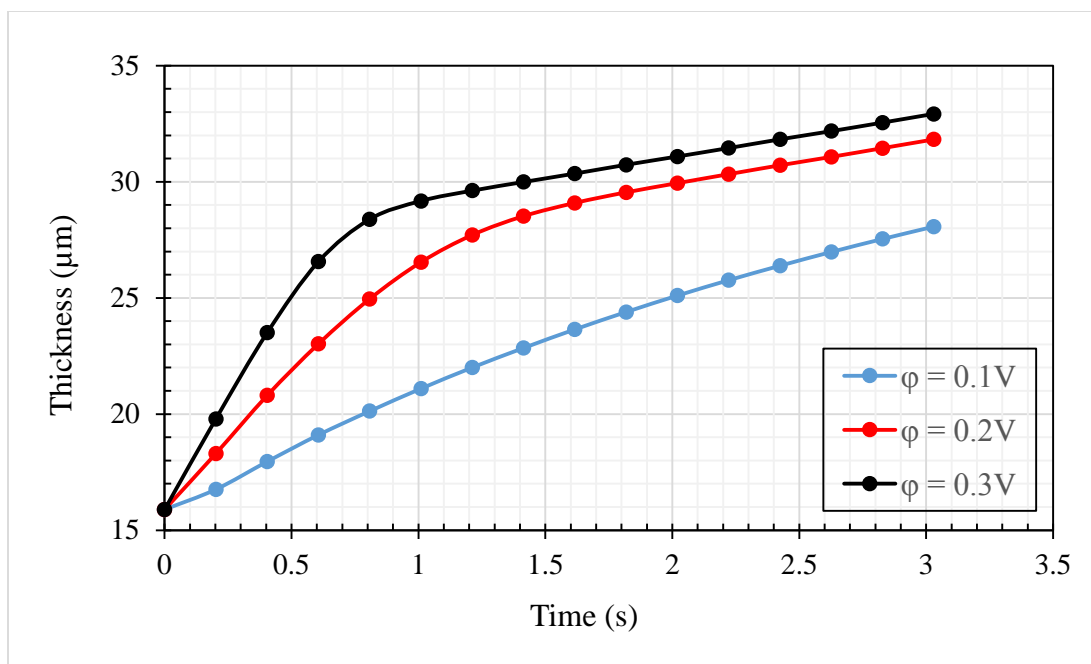


Figure 6.24. Thickness vs time for different voltages at  $0.05 \text{ mol/m}^2\text{s}$  flux

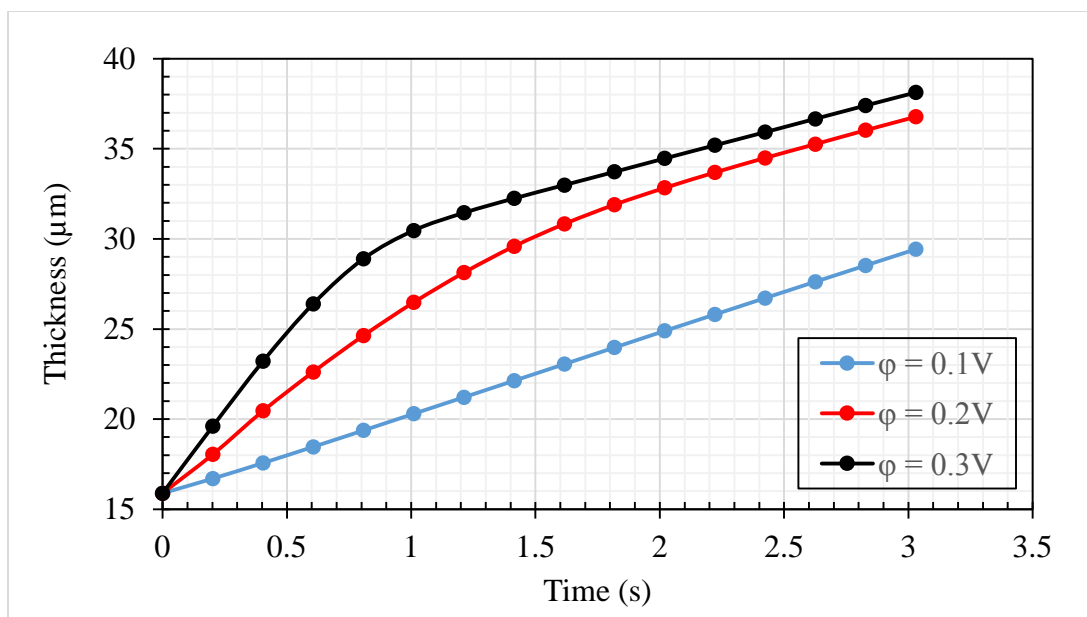


Figure 6.25. Thickness vs time for different voltages at  $0.1 \text{ mol/m}^2\text{s}$  flux

The values of growth thicknesses obtained after 3.03s for different applied voltages and different fluxes of concentration have been summarized in Table 6.2.

Growth thickness for different values of applied voltage and flux of concentration below:

Table 6.2. Growth thickness for different values of applied voltage and flux of concentration

Applied voltage (V)	Values of Flux		
	0.01 mol/m <sup>2</sup> s	0.05 mol/m <sup>2</sup> s	0.1 mol/m <sup>2</sup> s
0.1	25.43 μm	28.07 μm	29.42 μm
0.2	27.78 μm	31.82 μm	36.77 μm
0.3	28.74 μm	32.92 μm	38.12 μm

#### 6.4. COMPARISON WITH OTHER WORKS

In this work, the Laplace's equation is used as the governing equation for potential i.e. equation (16), which is

$$\nabla \cdot [\varepsilon(C) \nabla \phi] = 0$$

By maintaining the same governing equation for concentration, the governing equation for distribution of electric potential is varied as given in other works of phase field modeling for the electrodeposition process, to observe if there are any significant differences. A popular method that has been used to model the electrodeposition process is through the use of Butler-Volmer kinetics. This method was developed to include the

effects of reactions taking place at the electrode surfaces. Through basics of electrochemistry, it is understood that differences between activation energies of oxidation and reduction reactions cause variation in flow of current through an electrochemical system. The electrical current, taking into account the difference in activation energy between oxidation and reduction reactions using the Butler-Volmer kinetics can be described, as given in [63]:

$$\mathbf{i} = \mathbf{i}_{\text{ox}} - \mathbf{i}_{\text{red}} \quad (28)$$

$$\mathbf{i} = \mathbf{i}_{\text{ox}}^0 \exp\left(\frac{\alpha_{\text{sym}} F Z_M \eta}{RT}\right) - \mathbf{i}_{\text{red}}^0 \exp\left(-\frac{(1-\alpha_{\text{sym}}) F Z_M \eta}{RT}\right) \quad (29)$$

Where  $\mathbf{i}_{\text{ox}}^0$  and  $\mathbf{i}_{\text{red}}^0$  are the exchange current densities of the oxidant and the reductant respectively,  $\eta$  is the overpotential and  $\alpha_{\text{sym}}$  is the asymmetric parameter (i.e. transfer coefficient). A charge conservation equation is defined to solve for electric potential in the entire domain.

$$\nabla \cdot \mathbf{i} = 0 \quad (30)$$

The governing equation for distribution of electric potential as given by [63] is

$$\nabla \cdot \left[ \frac{\sigma_{A^-}^\beta}{F Z_{A^-}} \nabla (RT \ln C_M^\beta - F Z_{A^-} \phi) \right] = 0 \quad (31)$$

Where  $\sigma_{A^-}^\beta$  is the electrical conductivity of the domain and a function of phase field order parameter,  $Z_{A^-}$  is the charge number of the species and  $C_M^\beta$  is the concentration in the electrolyte. This is called the Poisson-Nernst-Planck (PNP) equation. A complete derivation of this equation can be found in [77]. For this study, (31) becomes

$$\nabla \cdot \left[ \frac{\varepsilon(C)}{Fz} \nabla (RT \ln C - Fz\phi) \right] = 0 \quad (32)$$

Using equations (14) and (32) as the governing equations to represent this model, the simulations are run for all cases as they were in Section 6.3. A comparison of growth thicknesses for different boundary conditions of concentration at different applied potentials, for different governing equations of electric potential is given in Table 6.3, Table 6.4 and Table 6.6.

Another method to describe the distribution of electric potential is by the use of a source term in the governing equation for potential to describe the change of charge density, which is a result of the reaction that takes place at the electrode face and this has been used in [65, 71]. It has been deliberated that this source term can describe the flow of current in the system due to cation motion in the electrolyte, electron motion in the electrode and electrochemical reaction at the electrode/electrolyte interface [65, 71]. The source term is a time dependent derivative of the evolution equation variable.

$$\nabla \cdot [\sigma(\xi) \nabla \phi] = \frac{i_0}{\lambda L_p} \frac{\partial \xi}{\partial t} \quad (33)$$

Where  $\sigma(\xi)$  is the phase parameter dependent electrical conductivity, given by  $\sigma(\xi) = \sigma_s p(\xi) + \sigma_L (1-p(\xi))$ ,  $\sigma_s$  and  $\sigma_L$  are the electrical conductivities of the electrode and electrolyte respectively,  $i_0$  is the exchange current density,  $L_p$  is the phase field mobility. The coefficient of the time dependent evolution term is a constant and varies only if the exchange current density,  $i_0$ , varies. Since the evolution equation in this study is a function of concentration, equation (33) is modified and written as

$$\nabla \cdot [\varepsilon(C) \nabla \phi] = (B) \frac{\partial C}{\partial t} \quad (34)$$

Where B is a constant equal to 0.01 in the non-dimensionalized space. Using (14) and (34) as governing equations, all the simulations were performed as done in Section 6.3. The following tables show comparison of growth thicknesses between each method for different boundary conditions of concentration and at different applied voltages.

Table 6.3. Comparison of growth thicknesses by using different forms of charge conservation equation for different boundary conditions and 0.1V applied voltage

Boundary Conditions & Time		Thickness ( $\mu\text{m}$ )		
Boundary Condition Of C	Time (s)	Laplace's equation	Poisson-Nernst-Planck equation	Time dependent evolution source term
Zero flux	1.616	23.36	23.37	23.39
Dirichlet	3.03	29.35	29.358	29.35
Flux of 0.01 mol/m <sup>2</sup> s	3.03	25.43	25.43	25.44
Flux of 0.05 mol/ m <sup>2</sup> s	3.03	28.07	28.06	28.07
Flux of 0.1 mol/ m <sup>2</sup> s	3.03	29.42	29.43	29.45



Table 6.4. Comparison of growth thicknesses by using different forms of charge conservation equation for different boundary conditions and 0.2V applied voltage

Boundary Conditions & Time		Thickness ( $\mu\text{m}$ )		
Boundary Condition Of C	Time (s)	Laplace's equation	Poisson-Nernst-Planck equation	Time dependent evolution source term
Zero flux	1.616	26.74	26.73	26.74
Dirichlet	3.03	44.46	44.46	44.46
Flux of 0.01 mol/ $\text{m}^2\text{s}$	3.03	27.78	27.78	27.78
Flux of 0.05 mol/ $\text{m}^2\text{s}$	3.03	31.82	31.82	31.82
Flux of 0.1 mol/ $\text{m}^2\text{s}$	3.03	36.77	36.77	36.77

Table 6.5. Comparison of growth thicknesses by using different forms of charge conservation equation for different boundary conditions and 0.3V applied voltage

Boundary Conditions & Time		Thickness ( $\mu\text{m}$ )		
Boundary Condition Of C	Time (s)	Laplace's equation	Poisson-Nernst-Planck equation	Time dependent evolution source term
Zero flux	1.616	27.68	27.68	27.68
Dirichlet	3.03	61.92	61.92	61.93
Flux of 0.01 mol/ $\text{m}^2\text{s}$	3.03	28.74	28.75	28.75
Flux of 0.05 mol/ $\text{m}^2\text{s}$	3.03	32.92	32.92	32.92
Flux of 0.1 mol/ $\text{m}^2\text{s}$	3.03	38.12	38.12	38.12

As seen in the above three tables, the values of growth thicknesses are almost the same even by using three different equations for the governing equation of electric potential. When plotted against each other, their values overlapped, giving no clear distinction between them since their values are almost the same. Although a macroscopic model has been used without closely studying the kinetics at the different surfaces in this work, this model gives almost the same growth thicknesses for different conditions as observed in the other models. This validates the use of the Laplace's equation in this work as a charge conservation equation, instead of the Poisson-Nernst-Planck equation or the time dependent evolution source term describing the current generated as the governing equation for electric potential.

## **6.5. EFFECT OF ANISOTROPY**

By considering a domain of  $63.56\mu\text{m} \times 25.42\mu\text{m}$  a single square seed of side length  $1.589\mu\text{m}$  on the surface of the electrode, simulations are performed a zero flux boundary condition for concentration and an applied voltage of  $0.3\text{V}$  on the right boundary of the domain. This seed represents a thermodynamically unstable region on the electrode surface. Figure 6.26 shows the concentration profile of a single seed on the surface of the anode when there is no applied voltage in the system. Physically, the seed represents a weak region of the solid electrolyte interface which has not adhered well to the anode surface and is more prone to phase changes compared to the other regions of the solid electrolyte interface. It should be noted that the figure mentions the time and length scales in the non-dimensionalized space. However, all the discussions will be made using real

values. Appendix C shows the difference of inputs in COMSOL Multiphysics for the case of anisotropy.



Figure 6.26. Single seed on the anode surface

It has been observed by Ely and Garcia [16] that the initial electrodeposits on the surface of a lithium anode takes place in the form of a spherical electrodeposit. The growth of this corresponding electrodeposit would depend on its critical radius and directional growth and microstructures can be observed only when the radius of the electrodeposit is larger than the critical radius of the electrodeposit. Though this work does not study the thermodynamics and kinetics of nucleation of these electrodeposits in detail, it can be seen from Figure 6.27 that this, in fact, occurs in lithium batteries. As time passes, the tip of the electrodeposit will be the most thermodynamically unstable region of the electrodeposit and growth rate is accelerated. As expected, the growth thicknesses and growth rates are very high at the end of the simulation. From an initial value of  $1.59\mu\text{m}$  at time  $t=0\text{s}$ , the growth thickness after just  $0.19\text{s}$  is  $15.37\mu\text{m}$ , which is almost 10 times the initial size. The growth rate at the end of the simulation is  $80.11\mu\text{m/s}$ . When compared with the growth

rates obtained in Section 6.3 for the same case of 0.3V applied voltage and zero flux of concentration (17.13  $\mu\text{m/s}$ ), this value is extremely large, thereby showing the propensity of the system to minimize its free energy faster in strongly anisotropic systems. Correspondingly, the current tip density will also be maximum at the tip of the lithium electrodeposit, in accordance with Ohm's law. If  $v_{\text{tip}}$  is the growth rate and  $V_m$  is the partial molar volume, then the tip current density is given by  $i_{\text{tip}} = v_{\text{tip}} zF/V_m$  [71]. Using this relation, tip current density at various time steps in the simulation can be calculated. Another factor for such rapid growth may also be due to the large concentration gradient present at the tip of the electrodeposit. A simpler way of looking at it is, since the  $\text{Li}^+$  ions flow towards the electrodeposit, the tip will first encounter highest concentration gradient, aiding in faster growth of the tip compared to other regions of the electrodeposit.

As discussed previously, the potential profile will still maintain three regimes. As the lithium electrodeposit i.e. solid phase grows, it will maintain the same uniform potential distribution as that of the electrode since both are made of lithium. The second region is at the interface where a gradient exists due to the accumulation of  $\text{Li}^+$  ions. The last region is at the right boundary where electrical conductivity of the system is the least. The potential profiles change according to the growth of the lithium electrodeposit and this is illustrated for different time steps in Figure 6.28.

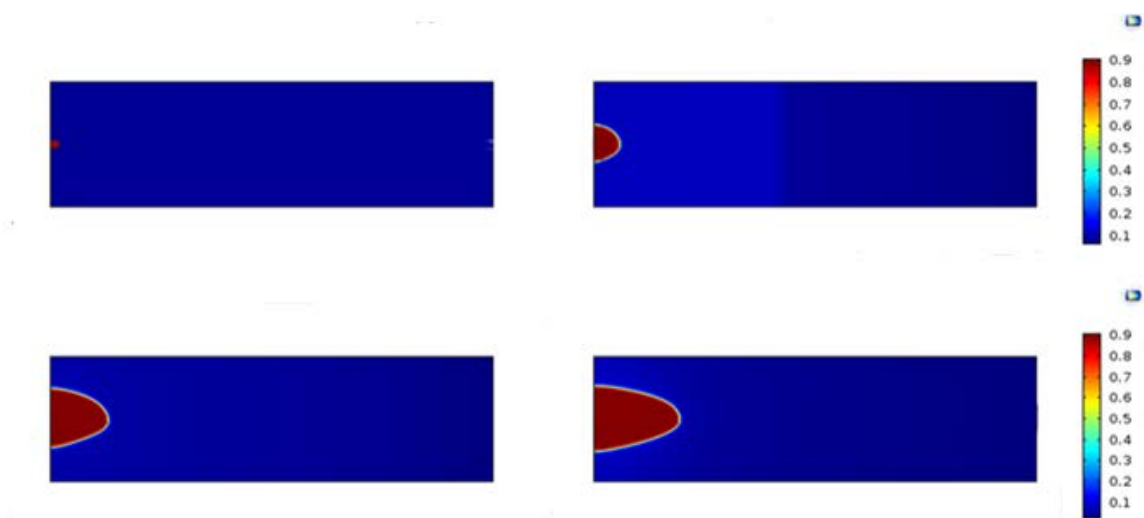


Figure 6.27. Anisotropic concentration profiles for  $t=0s$  and  $t=0.5s$  (top) and  $t=1s$  and  $t=1.9s$  (bottom) for zero flux of concentration and  $\phi=0.3V$

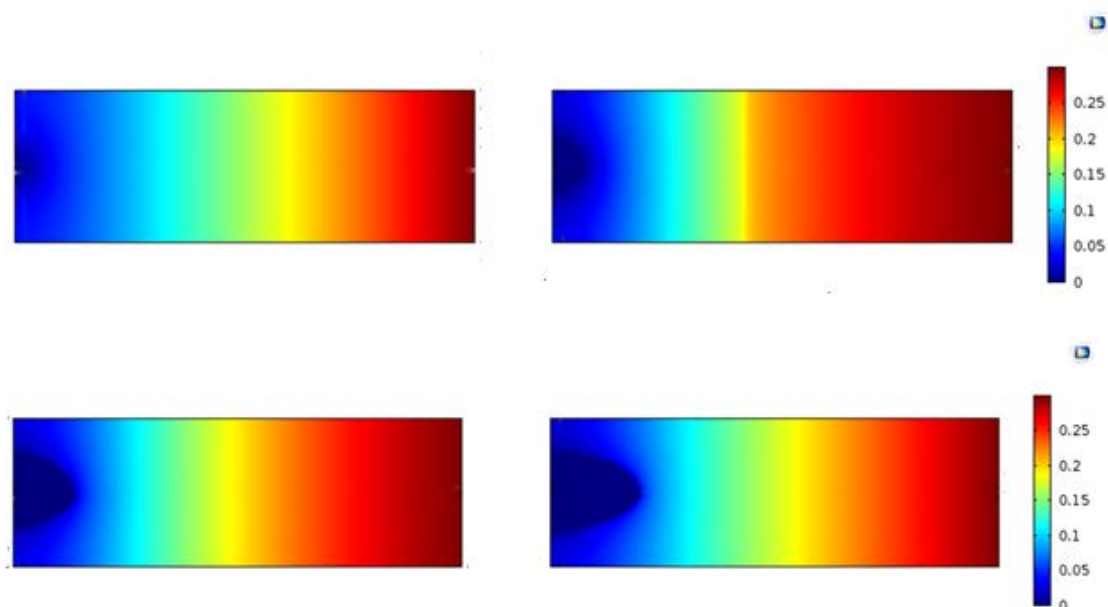


Figure 6.28. Anisotropic potential profiles for  $t=0s$  and  $t=0.5s$  (top) and  $t=1s$  and  $t=1.9s$  (bottom) for zero flux of concentration and  $\phi=0.3V$

A comparison with microstructure evolution in Li-ion batteries, presented in [71], is shown in Figure 6.29. This model uses an applied voltage of 0.2V in the system, whereas the model in this work uses 0.3V. Applied voltage does not affect any other parameter other than growth thickness. Higher the applied voltage, higher will be the growth thickness. The Li-ion battery model uses the order parameter as well, hence their model is a function of order parameter, concentration and distribution of electric potential, whereas our model uses only concentration and distribution of electric potential to define the free energy functional. Hence, the first row of figures in Figure 6.29 should be ignored while drawing a comparison between the two models. It can be seen that the concentration and potential profiles are very similar to those reported in Figure 6.27 and Figure 6.28.

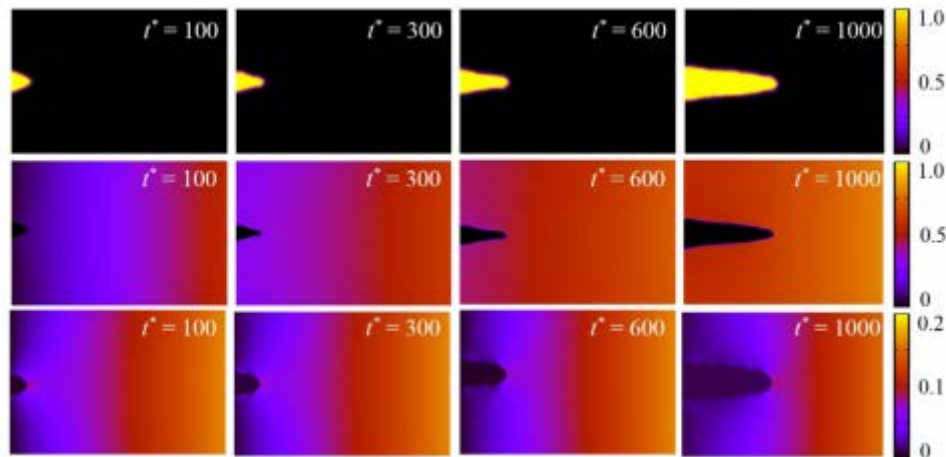


Figure 6.29. Snapshot of phase parameter (top),  $\text{Li}^+$  concentration (middle) and electric potential (bottom) profiles

## 6.6. DISCUSSIONS

Though the primary aspect of this work is microstructure simulations in lithium metal batteries using phase field modeling, it is worth noting that this work encompasses all the aspects related to lithium batteries, be it lithium metal or lithium-ion batteries. The detailed descriptions of emergence of lithium batteries as a major source of energy, not only in the present day, but also its prospects in the future has been reviewed. The transition of lithium battery technology from lithium metal batteries to lithium-ion batteries was the biggest measure taken to commercialize these batteries in 1991 and exploit the advantages of lithium as an energy storing material. However, as technologies advanced, there was an increasing need to revert back to lithium metal batteries as they provided over 10 times the energy density produced by Li-ion batteries. But the major roadblock has been the trade-off between energy density and operational safety, both of which should be high in a conventional battery. As the case with many technologies, the progress of research in this field has gone to the nanoscale to try and find solutions to this existing roadblock.

As the next step, a brief overview of different components of a lithium battery i.e. electrode, electrolyte components and solid electrolyte interface. Their advantages and limitations have also been highlighted so that optimum selection of components for the battery can be made based on the application. With this knowledge, the system chosen to model this work is a lithium metal anode, a  $\text{LiCoO}_2$  cathode immersed in a solution containing  $\text{LiPF}_6$  and a 1:1 ratio of a binary organic electrolyte consisting of ethylene chloride (EC) and dimethyl chloride (DMC). It should be noted that the components of the binary organic electrolyte are chosen such that the system has the most ideal values for operation. Also, the transition metal of the cathode, Co, is chosen such that the lithium cell

under consideration has the least drawbacks when compared to incorporation of other transition metals. It is again important to know that the selection of these components will depend on the application.

The importance of computational tools, not just for prediction of microstructures or materials science, but in all areas of science and engineering in today's world, is known. Computational techniques have taken over the modern world of research and industries since they provides a very cost-efficient way of understanding and developing a process. It is not only important for studying effects of certain parameters on a process, but CAD tools have made it possible to model even complex machine parts and then manufacture them. Another advantage of computational tools is the reduction of human error during initial experimentation. With knowledge of the outputs obtained from computation, one can easily perform experiments knowing the final result that needs to be obtained. This is also the case with Phase Field Modeling (PFM). It is a modification of the Finite Element Method (FEM), but is capable of simulating real-world processes at the mesoscopic length scale, unlike FEM. A comparison has been drawn between Phase Field Modeling and Sharp Interface Modeling techniques. Their advantages and drawbacks have been highlighted and it has also been shown that PFM requires lesser computational resources and time to model and simulate the growth of any microstructures, in that it would require only a single equation to define all the phases of a system without defining another equation to explicitly track the interface.

Since PFM has emerged as one of the strongest tools to compute and predict microstructures, it has been used in this work to model a lithium metal battery to understand the microstructure formation at the anode during charging process, which hinders safety



levels in these batteries. The aspects of PFM that have been used are described generally at first and then used to derive the governing equations used in this study. The free energy density and hence, the Ginzburg-Landau free energy functional have been defined as functions of concentration and electric potential only, whereas all the other works on PFM of electrodeposition process have been studied as functions of phase field order parameter, concentration and electric potential. Omitting the phase field order parameter does not make a difference to the output of the concentration and potential profiles. The order parameter is incorporated to show which part of the domain is in solid phase ( $\eta = 1$ ) and which part is in liquid phase ( $\eta = 0$ ). The variables in other studies have defined all functions such as electrical conductivity and diffusivity in terms of the order parameter, but all these functions have been defined as functions of concentration, as shown in Appendix B. All the electrochemical systems are driven by minimization of Gibbs free energy, where Gibbs free energy is a function of distribution of applied potential since the applied potential is the driving force for electrochemical reactions to occur in the battery. Figure 5.1 clearly shows that the growth of solid phase is preferred even when there is a small applied voltage of 0.1V.

The start of any phase field modeling work involves determining an optimum mesh size to discretize the domain into several grids. Simulations were performed for 7 different mesh sizes, starting from a coarse mesh of 0.25 and eventually using a very fine mesh of 0.04. The non-dimensionalized mesh size of 0.07 was determined to be most ideal and all further simulations were performed with a grid size of 0.07. Since the ratio of electrical conductivities of electrode and electrolyte in a lithium metal battery are extremely high ( $1 \times 10^7$ ), the computation was cumbersome and extremely long. Through simulations for 6

different electrical conductivity ratios between electrode and electrolyte, it has been shown that similar growth thicknesses were observed from a ratio of  $1 \times 10^4$  upto  $1 \times 10^7$ . It should be noted that using a conductivity ratio of  $1 \times 10^4$  instead of the original  $1 \times 10^7$  will not affect the profiles of any variable. It eases computation time to a certain extent, which is one of the main goals of all computational studies.

The behavior of the battery for different applied voltages and different conditions of concentration are studied and their results have been plotted and tabulated. To study the effect of applying 0.1V, 0.2V and 0.3V to a system with zero flux, Dirichlet and Neumann (3 cases) boundary conditions of concentration, a total of 45 cases were simulated. While some of these cases are impractical in real-world situations, the operational safety levels for different cases can be gauged from the growth thicknesses and the growth rates. A thorough linear dependence of higher applied voltage and high fluxes of concentration on the growth thickness of lithium electrodeposits has been established.

Different PFMs of electrodeposition mainly vary in the definition of the charge conservation equation i.e. the governing equation for distribution of electric potential. During modeling of electrochemical systems, one should bear in mind that if too much emphasis is laid on studying the thermodynamics and kinetics of the interfacial layer, then modeling of macroscopic systems (real-world systems) will be compromised as the equations are defined such that they capture the behavior of each and every component in the system and this is computationally very complex. Hence, many studies use Butler-Volmer kinetics, dilute solution approximation (use of a Laplace's equation) and Marcus-Hush kinetics to model macroscopic systems and study the behavior of major components in the system and the behavior of the interface. A comparison has been drawn to two other

popular PFMs of electrodeposition which use different source terms to define their charge conservation equation. Since this has been done for all the conditions mentioned in Section 6.3, a total of 45 cases were simulated. Comparison between the models yielded almost similar growth thicknesses. Hence, any of the three charge conservation equations can be used in the model presented in this work.

It is important to note that all the simulations until this point were run assuming that the system was isotropic in nature, which is an ideal case. Hence, the growth thicknesses obtained have been homogeneous and no microstructure formation is observed. But real-world systems are anisotropic in nature and the strength of anisotropy in each system can vary and most of them are strongly anisotropic. The surface energy defined is now a function of the strength of anisotropy and the crystallographic axis. This makes the electrodeposition process highly directional, thereby enabling growth in a particular direction which would result in different microstructures. Section 6.5 shows a detailed definition of the equations used and how the governing equation for concentration gets modified due to the inclusion of anisotropy.

## **6.7. FUTURE WORK**

Research in the field of lithium batteries is not only popular, but motivation to achieve further advances in it is gaining momentum every day. Such is the potential of pure lithium batteries. The future prospects of these batteries are immense. Since natural resources are depleting at such a rapid rate, the dependence on such energy technologies can only grow. The driving force behind this is the advancement in the field of materials science coupled with the development of more powerful computational tools. Chapter 1 gives descriptions of the future prospects of these batteries.

Unlike other phase field models that use a pure material as the anode, it should be observed that the electrolyte concentration used in this work is comparatively large. To give an example, in the electrodeposition of copper on a pure copper electrode presented in [64], the mole fractions of the electrode and electrolyte are considered to be 0.98 and 0.018 respectively. But in this work, the mole fractions used for the solid and liquid phases are 0.9 and 0.1 respectively, which are more tangible to real world applications.

Though so many cases of working of lithium metal batteries have been presented in this work, accelerated growth rates of the electrodeposits during the charging process, as seen in Section 6.5, coupled with high reactivity of pure lithium still render the use of these conventional lithium metal batteries as unsafe if the application necessitates its use over a long time. Hence, exploiting the high energy density of pure lithium metal still stands as a challenge even after a century of research in this field. Eliminating microstructure growth in any lithium battery technology is perhaps impossible at this point of time and all the studies are directed towards suppressing this growth from the anode surface. With the knowledge of some parameters like electrolyte concentration, free energy of formation, applied voltage that control evolution and fast growth of electrodeposits presented here, further advances in nanotechnology by using pure lithium with nanowires should be the next stage in reviving lithium metal battery technology and limiting microstructure growth.

APPENDIX A

NON-DIMENSIONALIZATION PROCEDURE

The technique of non-dimensionalization is particularly useful in systems that are defined by a set of partial differential equations. The equations in the coupled phase field model is complex to solve in real dimensions. They are converted to the dimensionless form enables us to simplify the problem and apply the appropriate techniques to solve them and gives us insight into the parameters that are important and those that can be treated approximately. In this phase field model, the parameters are non-dimensionalized during computation and then converted back to real units upon solving them.

The non-dimensional position,  $\bar{r}$ , and time,  $\bar{t}$ , are given by

$$\bar{r} = \frac{r}{r^*}, \text{ where } r^* = \sqrt{\frac{\beta_1}{W_1}}$$

$$\bar{t} = \frac{t}{t^*}, \text{ where } t^* = \frac{\beta_1}{DW_1}$$

The values are  $r^* = 3.178 \times 10^{-6} \text{ m} = 3.178 \mu\text{m}$  and  $t^* = 0.101 \text{ s}$

Using the above two equations, governing equation for concentration can be written as

$$\frac{\partial \bar{C}}{\partial \bar{t}} = \bar{M} \bar{\nabla}^2 \left[ \frac{\partial \bar{f}}{\partial \bar{C}} - \bar{\beta} (\bar{\nabla}^2 \bar{C}) \right]$$

Where

$$\bar{f} = \frac{f}{RT\Delta C}; \quad \bar{\nabla} = r^* (\nabla) \text{ and } \bar{M} = \frac{D}{RT\Delta C}$$

$$\bar{M} = 1$$

$\beta_1 = 500 * \beta = 5 \times 10^{-7} \text{ J/m}$ , where  $X = 500$

$W = 12.5 * (RT\Delta C) = 24.75 \times 10^3 \text{ J/m}^3$ , where  $Z = 12.5$

$$W_1 = 2W = 49.5 \times 10^3 \text{ J/m}^3, \text{ where } Y = 2$$

$$\text{Hence, } \bar{\beta} = \frac{Y^*Z}{X} = 0.05$$

The governing equation for potential can be written as –

$$\frac{1}{(r^*)^2} \bar{\nabla} \cdot [\varepsilon(C) \bar{\nabla} \phi] = 0$$

Therefore,

$$\bar{\nabla} \cdot [\varepsilon(C) \bar{\nabla} \phi] = 0$$

APPENDIX B  
INPUTS IN COMSOL MULTIPHYSICS



## 1. Parameters used in the simulation –

Parameters

▼ Parameters

Name	Expression	Value	Description
alphap	0.05	0.05	
C2	0.9	0.9	
sigmas	1e4 [S/m]	10000 S/m	
sigmal	1 [S/m]	1 S/m	
F	96500 [C/mol]	96500 C/mol	
R	8.314 [J/mol/K]	8.314 J/(mol·K)	
C1	0.1	0.1	
z	1	1	

## 2. Variables used in the simulation –

Variables

Label: Variables 1

Geometric Entity Selection

Geometric entity level: Entire model

ON

Active

Variables

Name	Expression	Unit
beta_hat	alphap	
T	298 [K]	K
W	12.5	
epsi	$1 * ((C - C2)^2 / (C1 - C2)^2) + 10000 * ((C - C1)^2 / (C2 - C1)^2)$	
A	$(C - C1)^2 / (C2 - C1)^2$	
B	$(C - C2)^2 / (C1 - C2)^2$	
f	$W * A * B + F * C * \text{phi} / (0.8 * R * T)$	
fc	$2 * L * ((C - C1)^2 * (C - C2) + (C - C2)^2 * (C - C1)) + F * \text{phi} / (0.8 * R * T)$	
L	$W / ((C2 - C1)^2 * (C1 - C2)^2)$	
fcx	$2 * L * (((C - C1)^2 * Cx + (C - C2)^2 * (C - C1) * Cx) + ((C - C2)^2 * Cx + (C - C1)^2 * (C - C2) * Cx)) + F * \text{phix} / (0.8 * R * T)$	1/m
fcy	$2 * L * (((C - C1)^2 * Cy + (C - C2)^2 * (C - C1) * Cy) + ((C - C2)^2 * Cy + (C - C1)^2 * (C - C2) * Cy)) + F * \text{phiy} / (0.8 * R * T)$	1/m

## 3. Governing equations –

## a) Governing equation for concentration

$$\frac{\partial C}{\partial t} = M \nabla^2 \left[ 10000C \cdot e^{-100(C+0.005)} + \frac{\partial f}{\partial C} - \beta (\nabla^2 C) \right]$$

▼ Equation

Show equation assuming:

Study 1, Time Dependent

$$e_a \frac{\partial^2 C}{\partial t^2} + d_a \frac{\partial C}{\partial t} + \nabla \cdot \Gamma = f$$

$$\nabla = \left[ \frac{\partial}{\partial x}, \frac{\partial}{\partial y} \right]$$

▼ Conservative Flux

$\Gamma$	$-(10000 \cdot Cx \cdot \exp(-100 \cdot (C+0.005))) + fcx - \text{beta\_hat} \cdot (px + qx)$	x	m
	$-(10000 \cdot Cy \cdot \exp(-100 \cdot (C+0.005))) + fcy - \text{beta\_hat} \cdot (py + qy)$	y	

▼ Source Term

$f$   1

▼ Damping or Mass Coefficient

$d_a$   s

▼ Mass Coefficient

$e_a$   s<sup>2</sup>

b) Governing equation for p –

$$p = \frac{\partial^2 C}{\partial x^2}$$

▼ Equation

Show equation assuming:

Study 1, Time Dependent ▼

$$e_a \frac{\partial^2 p}{\partial t^2} + d_a \frac{\partial p}{\partial t} + \nabla \cdot \Gamma = f$$

$$\nabla = \left[ \frac{\partial}{\partial x}, \frac{\partial}{\partial y} \right]$$

▼ Conservative Flux

$\Gamma$	Cx	x	1/m
	0	y	

▼ Source Term

$f$	p		1/m <sup>2</sup>
-----	---	--	------------------

▼ Damping or Mass Coefficient

$d_a$	0		s/m <sup>2</sup>
-------	---	--	------------------

▼ Mass Coefficient

$e_a$	0		s <sup>2</sup> /m <sup>2</sup>
-------	---	--	--------------------------------

c) Governing equation for  $q$  –

$$q = \frac{\partial^2 C}{\partial y^2}$$

▼ Equation

Show equation assuming:

Study 1, Time Dependent

$$e_a \frac{\partial^2 q}{\partial t^2} + d_a \frac{\partial q}{\partial t} + \nabla \cdot \Gamma = f$$

$$\nabla = \left[ \frac{\partial}{\partial x}, \frac{\partial}{\partial y} \right]$$

▼ Conservative Flux

$\Gamma$	<input type="text" value="0"/>	x	1/m
	<input type="text" value="Cy"/>	y	

▼ Source Term

$f$   1/m<sup>2</sup>

▼ Damping or Mass Coefficient

$d_a$   s/m<sup>2</sup>

▼ Mass Coefficient

$e_a$   s<sup>2</sup>/m<sup>2</sup>

d) Governing equation for distribution of electric potential –

$$\nabla \cdot [\varepsilon(C) \nabla \phi] = 0$$

▼ Equation

Show equation assuming:

Study 1, Time Dependent

$$e_a \frac{\partial^2 \phi}{\partial t^2} + d_a \frac{\partial \phi}{\partial t} + \nabla \cdot \Gamma = f$$

$$\nabla = \left[ \frac{\partial}{\partial x}, \frac{\partial}{\partial y} \right]$$

▼ Conservative Flux

$\Gamma$	<input type="text" value="epsi*phix"/>	x	$A/m^2$
	<input type="text" value="epsi*phiy"/>	y	

▼ Source Term

$f$    $A/m^3$



▼ Damping or Mass Coefficient

$d_a$    $s^4 \cdot A^2 / (kg \cdot m^5)$



▼ Mass Coefficient

$e_a$    $s^5 \cdot A^2 / (kg \cdot m^5)$

## 4. Solver type used –


Settings  

Fully Coupled

 Compute to Selected  Compute

Label:

▼ General

Linear solver:  

▼ Method and Termination

Nonlinear method:

Initial damping factor:

Minimum damping factor:

Restriction for step-size update:

Use recovery damping factor:

Recovery damping factor:


Termination technique:

Maximum number of iterations:

Tolerance factor:

▼ Results While Solving

Plot

Plot group:  

Probes:

## APPENDIX C

### INPUTS IN COMSOL MULTIPHYSICS FOR ANISOTROPY



The main changes in the inputs for the case of anisotropy is the variables and the governing equation for concentration, which are presented below:

### 1. Variables –

Variables		
Geometric Entity Selection		
Geometric entity level:		Entire model
<input checked="" type="checkbox"/> ON		
Active		
Variables		
Name	Expression	Unit
T	298 [K]	K
W	12.5	
epsi	$1 * ((C-C2)^2 / (C1-C2)^2) + 10000 * ((C-C1)^2 / (C2-C1)^2)$	
A	$(C-C1)^2 / (C2-C1)^2$	
B	$(C-C2)^2 / (C1-C2)^2$	
f	$W * A * B + F * C * \text{phi} / (0.8 * R * T)$	
fc	$2 * L * ((C-C1)^2 * (C-C2) + (C-C2)^2 * (C-C1)) + F * \text{phi} / (0.8 * R * T)$	
L	$W / ((C2-C1)^2 * (C1-C2)^2)$	
fcx	$2 * L * (((C-C1)^2 * Cx + (C-C2)^2 * (C-C1) * Cx) + ((C-C2)^2 * Cx + (C-C1)^2 * (C-C2) * Cx)) + F * \text{phix} / (0.8 * R * T)$	1/m
fcy	$2 * L * (((C-C1)^2 * Cy + (C-C2)^2 * (C-C1) * Cy) + ((C-C2)^2 * Cy + (C-C1)^2 * (C-C2) * Cy)) + F * \text{phiy} / (0.8 * R * T)$	1/m
theta	$\text{atan}(Cy / (Cx + 0.0001))$	rad
gamma	$1 + \text{delta} * \cos(4 * \text{theta})$	
delta	0.3	
gammap	$-4 * \text{delta} * \sin(4 * \text{theta})$	
P	$(Cx^2 + Cy^2)$	1/m <sup>2</sup>
Lx1	$((P + 0.0001)^{1/2} * (2 * Cy * Cxy - Cxx * Cy - Cxy * Cx) - (Cy^2 - Cx * Cy) * (0.5 * (P + 0.0001)^{-1/2} * (2 * Cx * Cxx + 2 * Cy * Cxy))) / (P + 0.0001)$	1/m <sup>2</sup>
Ly1	$((P + 0.0001)^{1/2} * (2 * Cx * Cxy - Cxy * Cy - Cyy * Cx) - (Cx^2 - Cx * Cy) * (0.5 * (P + 0.0001)^{-1/2} * (2 * Cx * Cxy + 2 * Cy * Cyy))) / (P + 0.0001)$	1/m <sup>2</sup>

## 2. Governing equation for concentration (C)

Equation

Show equation assuming:

Study 1, Time Dependent

$$e_a \frac{\partial^2 C}{\partial t^2} + d_a \frac{\partial C}{\partial t} + \nabla \cdot \Gamma = f$$

$$\nabla = \left[ \frac{\partial}{\partial x}, \frac{\partial}{\partial y} \right]$$

Conservative Flux

$\Gamma_x$	$-(10000 * C * \exp(-100 * (C + 0.005))) + f_{cx} - \beta_{hat} * (\gamma * (p_x + q_x) + \gamma_{map} * L_{x1})$	x	m
$\Gamma_y$	$-(10000 * C * \exp(-100 * (C + 0.005))) + f_{cy} - \beta_{hat} * (\gamma * (p_y + q_y) + \gamma_{map} * L_{y1})$	y	

Source Term

$f$  0 1

Damping or Mass Coefficient

$d_a$  1 s

Mass Coefficient

$e_a$  0 s<sup>2</sup>

**BIBLIOGRAPHY**

1. B. Scrosati, J.G., *Lithium Batteries: Status, Prospects and Future*. Journal of Power Sources, 2010. **195**: p. 2419-2430.
2. Chen, J., *Recent Progress in Advanced Materials for Lithium Ion Batteries*. Materials, 2013. **6**: p. 156-183.
3. Fergus, J.W., *Recent developments in cathode materials for lithium ion batteries*. Journal of Power Sources, 2010. **195**: p. 939-954.
4. J. M. Tarascon, M.A., *Issues and challenges facing rechargeable lithium batteries*. Nature, 2001. **414**: p. 359-367.
5. Kisuk Kang, Y.S.M., Julien Breger, Clare. P. Grey, Gerbrand Ceder, *Electrodes with High Power and High Capacity for Rechargeable Lithium Batteries*. Science, 2006. **311**(5763): p. 977-980.
6. P. Andrei, J.Z., M. Hendrickson, E. Plichta, *Some Possible Approaches for Improving the Energy Density of Li-Air Batteries*. Journal of the Electrochemical Society, 2012. **157**(12): p. A1287-A1295.
7. G. N. Lewis, F.G.K., *The Potential of the Lithium Electrode*. Journal of the American Chemical Society, 1913. **35**(4): p. 340-344.
8. Jasinski, R., *A summary of patents on organic electrolyte batteries*. Journal of Electroanalytical Chemistry and Interfacial Electrochemistry, 1970. **26**(2): p. 189-194.
9. Yeduvaka, G., R. Spotnitz, and K. Gering, *Macro-homogenous modeling of commercial, primary Li/MnO<sub>2</sub> coin cells*. ECS Transactions, 2009. **19**(16): p. 1-10.
11. Vincent, C.A., *Lithium batteries: a 50-year perspective, 1959–2009*. Solid State Ionics, 2000. **134**: p. 159-167.
12. Peled, E., *The Electrochemical Behavior of Alkali and Alkaline Earth Metals in Nonaqueous Battery Systems—The Solid Electrolyte Interphase Model*. Journal of the Electrochemical Society, 1979. **126**(2): p. 2047-2051.
13. Mizushima, K., et al., *Li<sub>x</sub>CoO<sub>2</sub> (0 < x ≤ 1): A new cathode material for batteries of high energy density*. Solid State Ionics, 1981. **3**: p. 171-174.
14. K. Mizushima, P.C.J., P.J. Wiseman and J.B. Goodenough, *A new Cathode Material for Batteries of High Energy Density*. Material Research Bulletin, 1980. **15**(6): p. 783-789.

15. Yuan, X., H. Liu, and J. Zhang, *Lithium-ion batteries: advanced materials and technologies*. 2011: CRC Press.
16. David. R. Ely, J.E.G., *Heterogeneous Nucleation and Growth of Lithium Electrodeposits on Negative Electrodes*. Journal of the Electrochemical Society, 2013. **160**(4): p. A662-A668.
17. Manthiram, A., Y. Fu, and Y.-S. Su, *Challenges and prospects of lithium–sulfur batteries*. Accounts of chemical research, 2012. **46**(5): p. 1125-1134.
18. Scheers, J., S. Fantini, and P. Johansson, *A review of electrolytes for lithium–sulphur batteries*. Journal of Power Sources, 2014. **255**: p. 204-218.
19. Bruce, P.G., et al., *Li-O<sub>2</sub> and Li-S batteries with high energy storage*. Nature materials, 2012. **11**(1): p. 19-29.
20. Abraham, K. and Z. Jiang, *A polymer electrolyte-based rechargeable lithium/oxygen battery*. Journal of The Electrochemical Society, 1996. **143**(1): p. 1-5.
21. Schulz, R., et al., *Recent developments in the applications of nanocrystalline materials to hydrogen technologies*. Materials Science and Engineering: A, 1999. **267**(2): p. 240-245.
22. Kraytsberg, A. and Y. Ein-Eli, *Review on Li–air batteries—Opportunities, limitations and perspective*. Journal of Power Sources, 2011. **196**(3): p. 886-893.
23. Christensen, J., et al., *A critical review of Li/air batteries*. Journal of the Electrochemical Society, 2011. **159**(2): p. R1-R30.
24. D. Aurbach, E.Z., H. Teller, P. Dan, *Factors Which Limit the Cycle Life of Rechargeable Lithium (Metal) Batteries*. Journal of the Electrochemical Society, 2000. **147**(4): p. 1274-1279.
25. Winter, M. in *Symposium on Large Lithium-ion Batteries and Applications (AABC)*. 2006.
26. J. B. Goodenough, Y.K., *Challenges for Rechargeable Li Batteries*. Chemistry of Materials, 2010. **22**(3): p. 587-603.
27. K. Tasaki, K.K., S. Nakamura and M. Ue, *Decomposition of LiPF<sub>6</sub> and Stability of PF<sub>5</sub> in Li-Ion Battery Electrolytes: Density Functional Theory and Molecular Dynamics Studies*. Journal of The Electrochemical Society, 2003. **150**(12): p. A1628-A1636.

28. Smith, O.B.a.G.D., *Quantum Chemistry and Molecular Dynamics Simulation Study of Dimethyl Carbonate: Ethylene Carbonate Electrolytes Doped with LiPF<sub>6</sub>*. Journal of Physical Chemistry B, 2009. **113**(6): p. 1763-1776.
29. Stephan, A.M., *Review on gel polymer electrolytes for lithium batteries*. European Polymer Journal, 2006. **42**: p. 21-42.
30. J. Hassoun, P.R., B. Scrosati, *Recent advances in liquid and polymer lithium-ion batteries*. Journal of Materials Chemistry, 2007. **17**: p. 3668-3677.
31. S. E. Sloop, J.K.P., S. Wang, J. B. Kerr, K. Kinoshita, *Chemical Reactivity of PF<sub>5</sub> and LiPF<sub>6</sub> in Ethylene Carbonate/Dimethyl Carbonate Solutions*. Electrochemical and Solid State Letters, 2001. **4**(4): p. A42-A44.
32. Chazalviel, J.-N., *Electrochemical aspects of the generation of ramified metallic electrodeposits*. Physical Review A, 1990. **42**: p. 7355.
33. C. Brissot, M.R., J.-N. Chazalviel, S. Lascaud, *Concentration measurements in lithium/polymer–electrolyte/lithium cells during cycling*. Journal of Power Sources, 2001. **94**(2): p. 212-218.
34. Xu, K., *Nonaqueous Liquid Electrolytes for Lithium-Based Rechargeable Batteries*. Chemical Reviews, 2004. **104**: p. 4303-4417.
35. V. Aravindan, J.G., S. Madhavi, Hua-Kun Liu, *Lithium-Ion Conducting Electrolyte Salts for Lithium Batteries*. Chemistry - A European Journal, 2011. **17**(51): p. 14326-14346.
36. Aurbach, D., et al., *The Study of Electrolyte Solutions Based on Ethylene and Diethyl Carbonates for Rechargeable Li Batteries II. Graphite Electrodes*. Journal of The Electrochemical Society, 1995. **142**(9): p. 2882-2890.
37. Zhang, S.S., K. Xu, and T.R. Jow, *Study of LiBF<sub>4</sub> as an electrolyte salt for a Li-ion battery*. Journal of The Electrochemical Society, 2002. **149**(5): p. A586-A590.
38. Schmidt, M., et al., *Lithium fluoroalkylphosphates: a new class of conducting salts for electrolytes for high energy lithium-ion batteries*. Journal of power sources, 2001. **97**: p. 557-560.
39. M. D. Bhatt, C.O.D., *Density functional theory calculations for ethylene carbonate-based binary electrolyte mixtures in lithium ion batteries*. Current Applied Physics, 2014. **14**(3): p. 349-354.
40. C.R. Yang, Y.Y.W., C.C. Wan, *Composition analysis of the passive film on the carbon electrode of a lithium-ion battery with an EC-based electrolyte*. Journal of Power Sources, 1998. **72**(1): p. 66-70.

41. McArthur, M., S. Trussler, and J. Dahn, *In situ investigations of SEI layer growth on electrode materials for lithium-ion batteries using spectroscopic ellipsometry*. Journal of The Electrochemical Society, 2012. **159**(3): p. A198-A207.
42. Reddy, T.B. and S. Hossain, *Rechargeable lithium batteries (ambient temperature)*. Handbook of batteries, 2002. **3**(11): p. 34.1-34.62.
43. Lian, P., et al., *Large reversible capacity of high quality graphene sheets as an anode material for lithium-ion batteries*. Electrochimica Acta, 2010. **55**(12): p. 3909-3914.
44. Zhao, X., et al., *In-Plane Vacancy-Enabled High-Power Si-Graphene Composite Electrode for Lithium-Ion Batteries*. Advanced Energy Materials, 2011. **1**(6): p. 1079-1084.
45. Tarascon, J.-M. and M. Armand, *Issues and challenges facing rechargeable lithium batteries*. Nature, 2001. **414**(6861): p. 359-367.
46. Whittingham, M.S., *Lithium batteries and cathode materials*. Chemical reviews, 2004. **104**(10): p. 4271-4302.
47. Fergus, J.W., *Recent developments in cathode materials for lithium ion batteries*. Journal of Power Sources, 2010. **195**(4): p. 939-954.
48. Antolini, E., *LiCoO<sub>2</sub>: formation, structure, lithium and oxygen nonstoichiometry, electrochemical behaviour and transport properties*. Solid State Ionics, 2004. **170**(3): p. 159-171.
49. Belov, D. and M.-H. Yang, *Failure mechanism of Li-ion battery at overcharge conditions*. Journal of Solid State Electrochemistry, 2008. **12**(7-8): p. 885-894.
50. Chen, L.-Q., *Phase-field models for microstructure evolution*. Annual review of materials research, 2002. **32**(1): p. 113-140.
51. Provatas, N. and K. Elder, *Phase-field methods in materials science and engineering*. 2011: John Wiley & Sons.
52. Caginalp, G. and W. Xie, *Phase-field and sharp-interface alloy models*. Physical Review E, 1993. **48**(3): p. 1897.
53. Karma, A., *Phase-field formulation for quantitative modeling of alloy solidification*. Physical Review Letters, 2001. **87**(11): p. 115701.
54. Kim, S.G., W.T. Kim, and T. Suzuki, *Phase-field model for binary alloys*. Physical review e, 1999. **60**(6): p. 7186.

55. Moelans, N., B. Blanpain, and P. Wollants, *An introduction to phase-field modeling of microstructure evolution*. Calphad, 2008. **32**(2): p. 268-294.
56. Singer-Loginova, I. and H. Singer, *The phase field technique for modeling multiphase materials*. Reports on Progress in Physics, 2008. **71**(10): p. 106501.
57. Steinbach, I., *Phase-field models in materials science*. Modelling and simulation in materials science and engineering, 2009. **17**(7): p. 073001.
58. Wheeler, A.A., W. Boettinger, and G. McFadden, *Phase-field model for isothermal phase transitions in binary alloys*. Physical Review A, 1992. **45**(10): p. 7424.
59. Mamivand, M., M.A. Zaeem, and H. El Kadiri, *A review on phase field modeling of martensitic phase transformation*. Computational Materials Science, 2013. **77**: p. 304-311.
60. Mamivand, M., M.A. Zaeem, and H. El Kadiri, *Phase field modeling of stress-induced tetragonal-to-monoclinic transformation in zirconia and its effect on transformation toughening*. Acta Materialia, 2014. **64**: p. 208-219.
62. Akolkar, R., *Mathematical model of the dendritic growth during lithium electrodeposition*. Journal of Power Sources, 2013. **232**: p. 23-28.
63. Okajima, Y., Y. Shibuta, and T. Suzuki, *A phase-field model for electrode reactions with Butler–Volmer kinetics*. Computational Materials Science, 2010. **50**(1): p. 118-124.
64. Shibuta, Y., Y. Okajima, and T. Suzuki, *Phase-field modeling for electrodeposition process*. Science and Technology of Advanced Materials, 2007. **8**(6): p. 511-518.
65. Zhang, H.-W., et al., *Understanding and Predicting the Lithium Dendrite Formation in Li-Ion Batteries: Phase Field Model*. ECS Transactions, 2014. **61**(8): p. 1-9.
66. Spatschek, R., et al., *Phase field modeling of fast crack propagation*. Physical review letters, 2006. **96**(1): p. 015502.
67. Koslowski, M., A.M. Cuitino, and M. Ortiz, *A phase-field theory of dislocation dynamics, strain hardening and hysteresis in ductile single crystals*. Journal of the Mechanics and Physics of Solids, 2002. **50**(12): p. 2597-2635.
68. Rowlinson, J., *Translation of JD van der Waals' "The thermodynamik theory of capillarity under the hypothesis of a continuous variation of density"*. Journal of Statistical Physics, 1979. **20**(2): p. 197-200.
69. Guyer, J., et al., *Phase field modeling of electrochemistry I: Equilibrium*. arXiv preprint cond-mat/0308173, 2003.

70. Guyer, J., et al., *Phase field modeling of electrochemistry. II. Kinetics*. Physical Review E, 2004. **69**(2): p. 021604.
71. Liang, L. and L.-Q. Chen, *Nonlinear phase field model for electrodeposition in electrochemical systems*. Applied Physics Letters, 2014. **105**(26): p. 263903.
72. Cogswell, D.A., *Quantitative phase-field modeling of dendritic electrodeposition*. Physical Review E, 2015. **92**(1): p. 011301.
73. Laborda, E., et al., *A comparison of Marcus–Hush vs. Butler–Volmer electrode kinetics using potential pulse voltammetric techniques*. Journal of Electroanalytical Chemistry, 2011. **660**(1): p. 169-177.
74. Qin, R. and H. Bhadeshia, *Phase field method*. Materials science and technology, 2010. **26**(7): p. 803-811.
75. Torabi, S., et al. *A new phase-field model for strongly anisotropic systems*. in *Proceedings of the Royal Society of London A: Mathematical, Physical and Engineering Sciences*. 2009. The Royal Society.
76. Wise, S., J. Kim, and J. Lowengrub, *Solving the regularized, strongly anisotropic Cahn–Hilliard equation by an adaptive nonlinear multigrid method*. Journal of Computational Physics, 2007. **226**(1): p. 414-446.
77. Schuss, Z., B. Nadler, and R.S. Eisenberg, *Derivation of Poisson and Nernst-Planck equations in a bath and channel from a molecular model*. Physical Review E, 2001. **64**(3): p. 036116.



## VITA

Nihal Acharya was born on February 20, 1991 in Bangalore, India. He received his Bachelor's degree in Mechanical Engineering from M. S. Ramaiah Institute of Technology in Bangalore, India in June 2013. Upon completion of his Bachelor's degree, he was accepted in the MS program in Materials Science & Engineering at Missouri University of Science and Technology in Rolla, MO in August 2013. He carried out his research under the guidance of Dr. Mohsen Asle Zaem. He received his Master's degree in Materials Science & Engineering in May 2016.